Geological Magazine

www.cambridge.org/geo

Structural, lithostratigraphic and thermal features of a Permian lower crust from the Western Italian Alps (Valpelline Series, Valle d'Aosta)

Fabiola Caso, Antonella Strambini and Michele Zucali

Dipartimento di Scienze della Terra "A. Desio", Università degli Studi di Milano, Milano, Italy

Original Article

Cite this article: Caso F, Strambini A, and Zucali M (2024) Structural, lithostratigraphic and thermal features of a Permian lower crust from the Western Italian Alps (Valpelline Series, Valle d'Aosta). *Geological Magazine* **160**: 1983–2009. https://doi.org/10.1017/S0016756824000037

Received: 18 July 2023
Revised: 27 December 2023
Accepted: 8 January 2024
First published online: 6 February 2024

Keywords:
partial melting; migmatite; high-temperature metamorphism; Austroalpine

Corresponding author:
Fabiola Caso; Email: fabiola.caso@unimi.it

Abstract

The Valpelline Series (Dent-Blanche Tectonic System, Western Italian Alps) is a sector of lower continental crust, which consists of Permian migmatitic metapelite with different mineral assemblages (i.e., garnet-, cordierite- and orthopyroxene-bearing), minor amphibolite and marble, intruded by aplite and pegmatite. Widespread melt production in metapelite and locally in amphibolite occurred during the development of the regional foliation. The *P*–*T* conditions during migmatisation, estimated using conventional geothermobarometers, range between 800–900 °C and 0.5–0.8 GPa, with a difference of up to ~50 °C between cordierite- and orthopyroxene-bearing migmatites, the latter reaching higher temperatures. The Valpelline Series shows rock types, metamorphic assemblages, *P*–*T* conditions and published ages of high-temperature regional metamorphism like the archetypal lower crust section of the Ivrea-Verbano Zone in the Southern Western Alps. The latter likely represents an external portion of the same extending lower crust, at the onset of the Tethyan rifting due to lithospheric extension and asthenospheric rising.

1. Introduction

Investigating the tectono-metamorphic evolution of exposed amphibolite- to granulite-facies rocks is crucial for understanding the formation and evolution of the middle- to lower continental crust (Bohlen, 1987; Hacker *et al.* 2015; Touret *et al.* 2022) within different geodynamic settings, i.e., from collisional-related crustal thickening to post-collisional or back-arc lithospheric thinning (Jiao *et al.* 2023 and references therein). In these deeper crustal sectors, melt production and migration contribute to the growth and differentiation of the continental crust, shaping its composition and structure and influencing the deformation regime (Hawkesworth *et al.* 2020). Comprehending the litho-structural features of the lower continental crust is an important first step for the implementation of *P*–*T*–D–t paths and geochemical surveys to unveil crustal differentiation processes and provide insights into their tectonic framework.

In the Western Alps, there are pre-alpine lower crustal slices such as the II Zona Diorito-Kinzigitica (IIDK; Carraro *et al.* 1970), the Ivrea-Verbano Zone (IVZ; Quick *et al.* 2003; Redler *et al.* 2012, 2013; Ewing *et al.* 2013, 2015) and the Valpelline Series (VP; Gardien *et al.* 1994; Manzotti & Zucali, 2013; Caso, 2023), which have been affected by widespread high-temperature (hereafter H*T*) metamorphism and are now fragmented and found in different portions of the Western Alpine belt. The H*T* evolution is related to the post-Variscan collisional collapse and/or Permian lithospheric extension (Lardeaux & Spalla, 1991; Marotta & Spalla, 2007; Schuster & Stüwe, 2008; Roda *et al.* 2018; Roda *et al.* 2023). In particular, the VP in the Dent-Blanche Tectonic System (DBTS; Manzotti *et al.* 2014; Manzotti & Ballèvre, 2017), located in the Valle d'Aosta (Western Italian Alps), represents a well-preserved exposure of a lower continental crustal section that has largely escaped the Alpine-age metamorphic overprint. The VP is traditionally compared to the IVZ and the IIDK, all of which are part of the Adria paleomargin. This comparison is based on lithological affinities and similar dominant H*T* pre-alpine tectono-metamorphic imprint. In the past decades, several works have dealt with the H*T* evolution of the VP (Diehl *et al.* 1952; Gardien *et al.* 1994; Manzotti & Zucali, 2013) but they lack a detailed description and distinction of the different rock types and structures or they are localised to restricted areas of the unit (Diehl *et al.* 1952; Nicot, 1977; Pennacchioni & Guermani, 1993; Gardien *et al.* 1994; Manzotti & Zucali, 2013). Therefore, this contribution provides a detailed meso- and microscale description of VP rocks and their relations with the deformation history. Preliminary *P*–*T* estimations related to H*T* metamorphism and melt-production stages have been obtained both from metapelite and metabasite. A first characterisation of the thermal structure of the VP is provided, discussing the implications for the thermal conditions of the

extended Permian lithosphere. Ultimately, a preliminary comparison between the VP and the IVZ crustal section is given: it compares lithologies, structures, thermal conditions and available ages of metamorphism and magmatism discussing them within the regional context.

1.a. Geological setting

The Western Alps (Fig. 1a) originated from the subduction of the Jurassic Ligurian Piedmont Ocean and subsequent collision between the Adriatic and European plates from Cretaceous to Eocene times (Schmid *et al.* 2004; Beltrando *et al.* 2010; Angrand & Mouthereau, 2021). The Western Alps consist of three main structural domains (Bousquet *et al.* 2008): (i) the southern external domain, corresponding to the Adria-derived domains, i.e., the Southern Alps; (ii) the external domain, representing the European foreland (Helvetic domain) and (iii) the axial zone between the Penninic Front to the north and the Insubric Line to the south (Schmid *et al.* 1989; Handy *et al.* 2010). The axial zone includes remnants of the subducted oceanic lithosphere of the Piedmont–Ligurian Ocean (i.e., Piedmont Zone; Pognante, 1979; Dal Piaz, 1999; Zanoni *et al.* 2016; Luoni *et al.* 2020; Caso *et al.* 2021) and the continental crust of Adria (Giuntoli & Engi, 2016; Austroalpine Domain) and European pertinence (Penninic Domain). The DBTS (Manzotti *et al.* 2014; Manzotti & Ballèvre, 2017) is a continental klippe of the Austroalpine domain, which is divided into the Dent-Blanche s.s. to the northwest and the Mont-Mary Nappe (Fig. 1b) to the southwest separated by the Rosain-Cignana Shear Zone (Fig. 1b; Manzotti *et al.* 2014). The Dent-Blanche s.s. is composed of a Paleozoic basement corresponding to the Arolla and the Valpelline series (Argand, 1906; Diehl *et al.* 1952; Manzotti & Zucali, 2013; Manzotti *et al.* 2014). The Alpine-aged metamorphism is more pervasive in the Arolla Series ranging from greenschist- to blueschist-facies conditions (Roda & Zucali, 2008; Manzotti *et al.* 2020), while in the VP, the overprint is weak and localised in decametric- to hectometric deformation zones. The pre-alpine metamorphism is mostly preserved in the VP and is related to Variscan and post-Variscan evolution of H*T* and pressures conditions, ranging from kyanite to sillimanite stability field (Gardien *et al.* 1994; Manzotti & Zucali, 2013).

The VP consists of high-grade gneiss and migmatites associated with pegmatitic dikes, lenses of Grt–Cpx-amphibolite, basic granulite and marble (Diehl *et al.* 1952; Nicot, 1977; Gardien *et al.* 1994; Manzotti & Zucali, 2013). Regarding the pre-Alpine evolution, the first recognised tectono-metamorphic event (pre-D_2, T = 700 ± 50 °C and P = 0.57 ± 0.11 GPa; Manzotti & Zucali, 2013) is marked by a relict $S_{pre\text{-}2}$ foliation (referring to Manzotti & Zucali, 2013 nomenclature of the foliations and stages) preserved within metabasite and marble boudins enclosed within metapelite. Gardien *et al.* (1994) detected the oldest stage preserved within garnet cores and in the kyanite stability field (T = 700–800 °C and P = 0.9–1.0 GPa). The $S_{pre\text{-}2}$ foliation, developed during the pre-D_2 stage and preserved in the metabasic boudins, is wrapped by the S_2 foliation. The S_2 foliation developed during the subsequent D_2 stage and is associated with melt production (T = 810 ± 40 °C and P = 0.7 ± 0.01 GPa; Gardien *et al.* 1994; Manzotti & Zucali, 2013). The D_2 stage has been dated to Permian (Zucali *et al.* 2011; Pesenti *et al.* 2012; Kunz *et al.* 2018). During the D_3 stage (T = 800 ± 30 °C and P = 0.6 ± 0.07 GPa; Manzotti & Zucali, 2013), the S_2 is deformed by isoclinal folds, leading to the local development of an S_3 axial plane foliation, marked by the growth of biotite and sillimanite, both at the meso- and microscale. Gardien *et al.* (1994) constrained the D_3 event linked to the biotite–sillimanite S_3 foliation at T = 750–800 °C and P = 0.55–0.6 GPa. Moreover, they recognised a further migmatitic stage related to the cordierite growth, estimated at T = 650–700 °C and P = ~0.35–0.45 GPa. S_2 and S_3 are parallel to the lithological boundaries, strike NE-SW and dip at high-angle (Manzotti & Zucali, 2013). The D_4 stage is locally associated with the development of a mylonitic foliation (S_4) marked by chlorite and white mica, under greenschist-facies conditions at T = 430 ± 30 °C and P = 0.3–0.5 GPa (Gardien *et al.* 1994; Manzotti & Zucali, 2013). Locally, faults and cataclastic rocks related to brittle deformation also occur (Pennachioni & Guermani, 1993; Roda & Zucali, 2008; Manzotti & Zucali, 2013).

2. Materials and methods

The relative chronology of the tectono-metamorphic stages has been inferred by combining meso- and microstructural analysis, considering the geometric relationships between different structural elements (Passchier & Trouw, 2005; Spalla *et al.* 2005). The deformation phases are named using a numerical progression (e.g., D_1, D_2, etc.), in which S- indicates foliations, A- fold axes and a.p. axial planes. Metamorphic assemblages linked to each D- stage have been inferred correlating each mineral phase with their respective structural element, following the guidelines of Johnson and Vernon (1995), Passchier and Trouw (2005) and Spalla *et al.* (2005). Different mineral generations have been distinguished using a numerical progression (e.g., Bt I, Bt II, etc.) to emphasise the chronological relationships between minerals and structures. Mineral abbreviations used in the description, except for Wm (white mica) and Oamp (orthoamphibole), are after Whitney and Evans (2010).

Major elements whole-rock compositions have been acquired by the ICP–AES (Inductively Coupled Plasma Atomic Emission Spectroscopy) at 'Bureau Veritas Minerals' laboratories in Vancouver (Canada) and through FUS–ICP (Fusion-Inductively Coupled Plasma Mass) at Activation Laboratories LTD. in Ontario (Canada). Some compositions have been obtained by combining modal estimations from optical microscope observation and mineral compositions from the literature (e.g., Nicot, 1977; Manzotti & Zucali, 2013). Moreover, data from Nicot (1977) and Diehl *et al.* (1952) acquired through X-ray fluorescence have been also reported. All the analyses are in Supplementary Material 1 available online.

Mineral chemical analysis has been performed through a Jeol JXA-8200 Superprobe WDS (wavelength-dispersive spectrometer, accelerating voltage of 15 kV, beam current of 15 nA) operating at the Dipartimento di Scienze della Terra 'Ardito Desio' – Università degli Studi di Milano (Italy). For trace-element analyses in rutile (i.e., Zr, Cr, V, Nb, U, Y, Fe, Al and Si), a beam current of 100 nA has been used. The calculation of interference between V and Ti and V and Cr has been also applied. Mineral formulae have been calculated using pyMin v.2023 (Zucali, 2023), which uses the recalculation rules of Deer *et al.* (1996). Amphiboles are classified according to Hawthorne *et al.* (2012) classification, and pyroxenes after Morimoto *et al.* (1988). Structural formulae have been calculated on the basis of 22 oxygens for biotite, 12 for garnet, 8 for plagioclase, 23 for amphibole, 6 for pyroxene and 18 for cordierite. FeO_{tot} accounts for FeO and Fe_2O_3. X_{Mg} is defined as $Mg/(Mg+Fe^{2+})$ for biotite.

https://doi.org/10.1017/S0016756824000037 Published online by Cambridge University Press

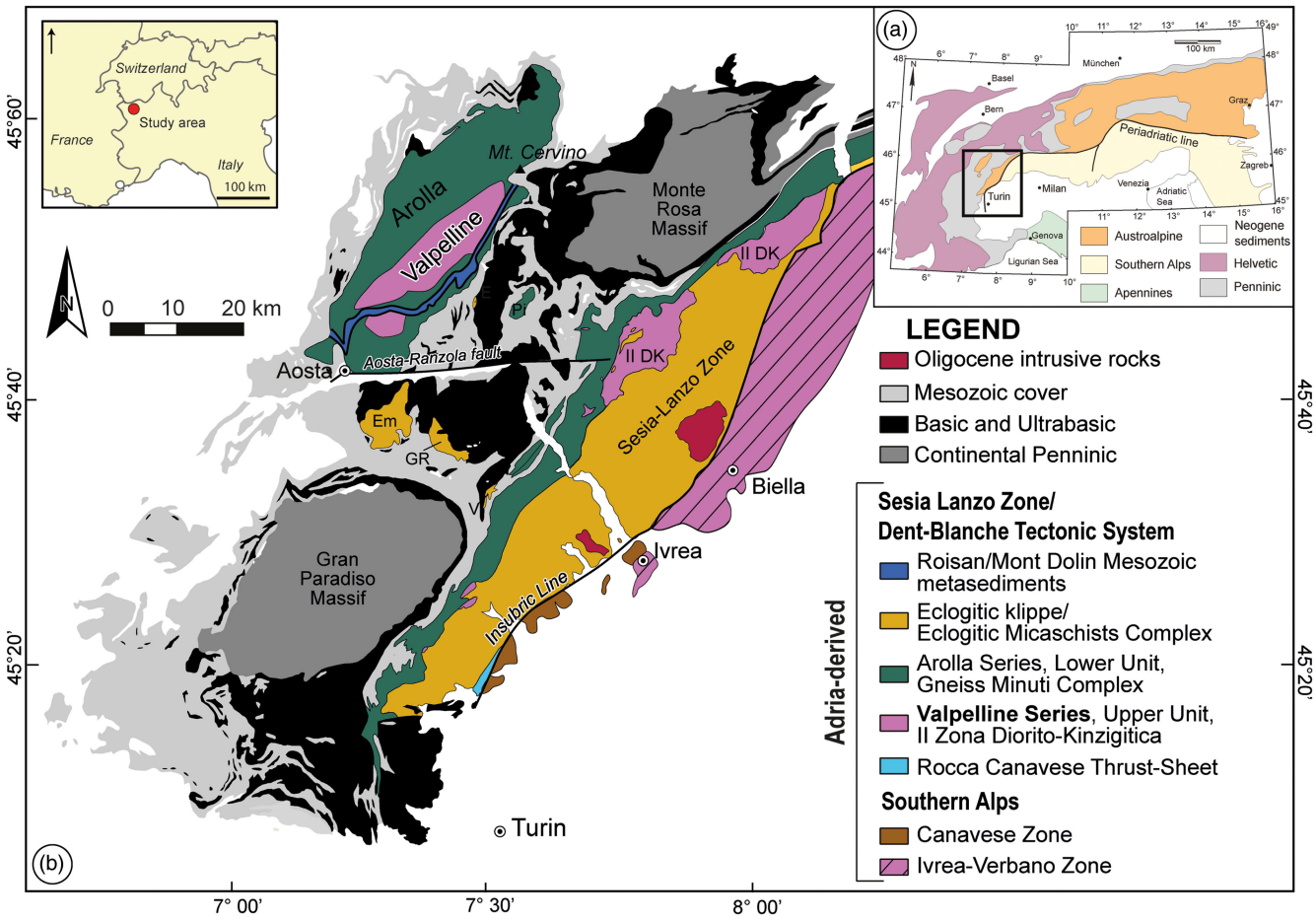

Figure 1. (Colour online) (a) Tectonic sketch map of the Alps showing the main palaeogeographic domains. (b) Geological map of the Western Alps highlighting the Adria-derived tectono-metamorphic units (modified after Roda *et al.* 2021). E: Etirol-Lèvaz; Em: Emilius; GR: Glacier Refray; Pi: Pillonet; V: Vanoise; IIDK: II Zona Diorito-Kinzigitica (Dent-Blanche s.s. and MM s.s. have not been differentiated).

3. Rock types

The VP is dominated by metapelites, with subordinated metabasite and metacarbonatic rocks occurring as lenses within metapelites or interlayered with them (Fig. 2). The lithologies have also been discriminated due to their mineralogy (Fig. 3a and b and Table 1) and bulk rock chemical variations.

3.a. Metapelite

3.a.1 Migmatite gneiss

Migmatite gneiss covering ~43 % of the VP at the map-scale (Fig. 2; Table 1) can be divided into four sub-types: (i) biotite + garnet + sillimanite-migmatite gneiss; (ii) biotite + garnet + sillimanite ± **cordierite**-migmatite gneiss; (iii) biotite + garnet + sillimanite ± **orthopyroxene**-migmatite gneiss and (iv) fine-grained biotite-migmatite gneiss (Table 1).

Bt+Grt+Sil-migmatite gneiss is the most abundant sub-type, occurring as metric to decametric outcrops, interlayered with black amphibolite, sillimanite-gneiss, felsic granulite and marble. They show a gneissic structure made by a regular layering between millimetric- to pluricentimetric-thick brownish domains of biotite, garnet and sillimanite (i.e., melanosomes) and pluricentimetric-thick white quartz-feldspathic leucosomes (Fig. 4a and b). Melanosomes constitute a continuous to locally spaced foliation, defined by the elongation of biotite and sillimanite crystals making mm-thick layers. Leucosomes constitute plurimillimetric- to pluricentimetric-thick levels, locally appearing as lens-shaped decimetric pods wrapped by the melanosomes or cutting the main foliation. In some outcrops, they wrap decimetric fine-grained metabasic lenses. In detail, leucosomes are made of fine-grained quartz, plagioclase and garnet (blue star in Fig. 4a); locally centimetric K-feldspar occurs (red star in Fig. 4a). The modal abundance of sillimanite in melanosomes varies across the outcrops, with some nearly devoid or dominated by biotite. Conversely, in some locations, sillimanite modal abundance and grain size increase, reaching up to 2 mm in length. At the microscale, the gneissic structure of migmatite is defined by the isorientation of idiomorphic millimetric biotite and fibrous to locally prismatic sillimanite (Fig. 4b) with minor ilmenite. Biotite locally occurring as larger deformed relict grains shows an intense reddish-brown colour and very fine-grained inclusions of rutile. Garnet commonly displays rounded inclusions of biotite, quartz, sillimanite and minor plagioclase, K-feldspar and rutile, concentrated in the core. Garnet is wrapped by the biotite + sillimanite-rich main foliation. Relict deformed biotite and fibrous sillimanite, with quartz films in between, are present in microsites within

https://doi.org/10.1017/S0016756824000037 Published online by Cambridge University Press

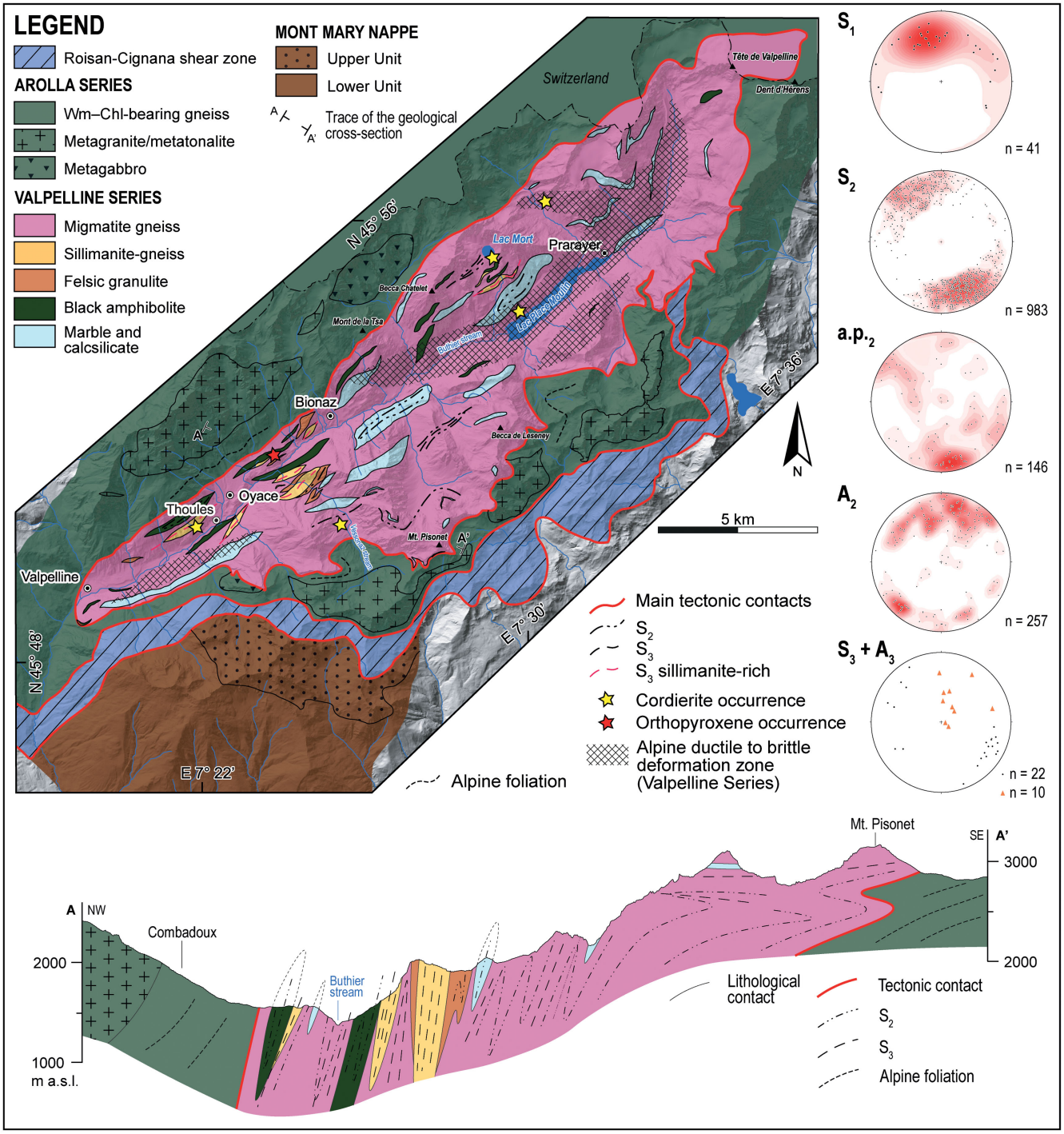

Figure 2. (Colour online) Schematic geological map showing the main units of the Dent-Blanche Tectonic System and the equal area stereographic projection of the main structural elements. At the bottom, geological cross-section (A – A') across the Arolla and Valpelline series.

skeletal garnet porphyroblasts. In some samples, garnet appears as anhedral millimetric blasts forming intergrowths with lobate quartz. The latter commonly shows a granoblastic structure with triple junctions in the less deformed or annealed leucosomes. A 'chessboard' structure is visible in the high-strain domains indicating deformation temperatures >700 °C (Stipp *et al.* 2002; Law, 2014). Quartz also forms irregular sub-millimetric to millimetric films among grain boundaries, such as garnet or biotite. Plagioclase in leucosomes is idiomorphic and sub-millimetric to plurimillimetric, often showing a sharp undeformed twinning. It is in mutual contact with quartz and when present, K-feldspar.

At the Lac Mort area (N 45°55'8" E 7°29'8" WGS84; Fig. 2), the aspect of migmatite gneiss is slightly different: the structure becomes more complex with folded leucosomes forming a ptygmatic structure. Moreover, the number of metabasite lenses

https://doi.org/10.1017/S0016756824000037 Published online by Cambridge University Press

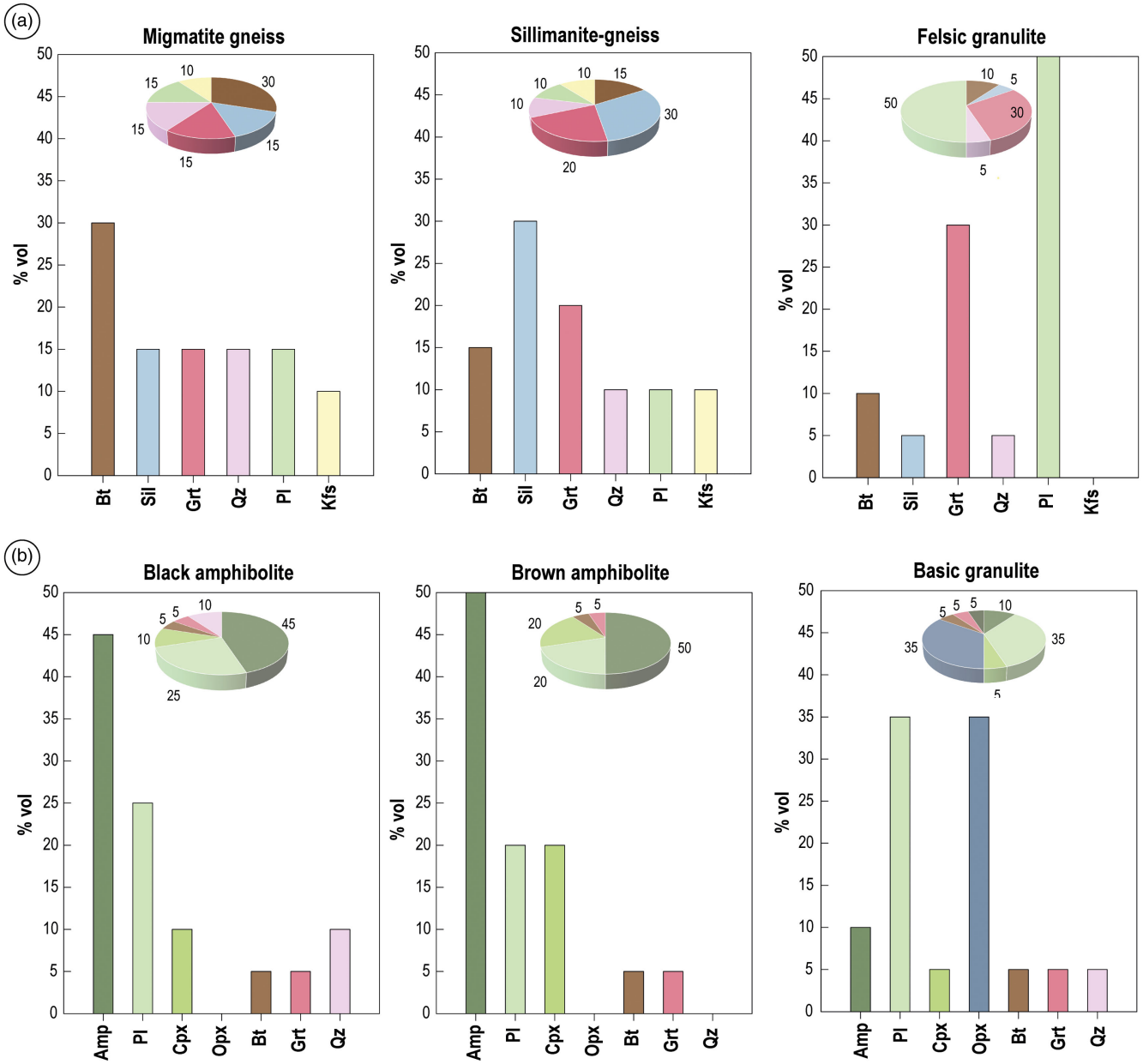

Figure 3. (Colour online) (a) Modal percentages (% vol) in metapelites and (b) metabasites.

and aplitic or pegmatitic dykes here increases. Sillimanite, which together with biotite highlights the main foliation, is fine-grained (~1 mm in length) with a fibrous habit.

The second sub-type of migmatite gneiss, Bt+Grt+Sil±**Crd**-migmatite gneiss, crops in a few spots along the valley (see yellow stars in Fig. 2). Cordierite appears as dark grey porphyroblasts of up to 3 cm within leucosomes or in the melanosomes wrapped by the biotite + sillimanite-rich foliation (Fig. 4c). At the microscale, cordierite is sub-idiomorphic or interstitial, millimetric to plurimillimetric in size, showing widespread fractures along which fine-grained aggregates of white mica and chlorite occur (Fig. 4d). It includes sub-millimetric rounded quartz, biotite and sillimanite. Moreover, cordierite (as well as garnet) is locally overgrown by late-stage biotite and sillimanite.

Bt+Grt+Sil±**Opx**-migmatite gneiss (Fig. 4e) crops out in one locality in the valley (N 45°51'55"; E 7°24'13"; red star in Fig. 2). These rocks show a gneissic structure defined by the alternance of discontinuous millimetric biotite-rich layers and plurimillimetric to pluricentimetric leucosomes. Plurimillimetric green to grey orthopyroxene porphyroblasts occur mostly in the leucosomes, together with garnet, and are wrapped by the biotite foliation (Fig. 4f). Sillimanite modal abundance is lower with respect to the other migmatite gneiss types. At the microscale, the foliation forms slightly discontinuous layers mainly made of biotite lamellae wrapping leucosomes. Orthopyroxene is characterised by the presence of rounded inclusions of quartz and biotite. Locally, biotite forms millimetric symplectitic intergrowths with quartz, wrapping or growing over orthopyroxene porphyroblasts.

Fine-grained Bt-migmatite gneiss occurs as metric to plurimetric-thick bodies (not visible at the map-scale), defining domains alternating with biotite + sillimanite-rich foliation and leucosomes or folded decimetric levels within Bt+Grt+Sil-

https://doi.org/10.1017/S0016756824000037 Published online by Cambridge University Press

Table 1. Summary of the main features of the rock types cropping out in the VP.

System	Group	Lithology	Modal composition	Texture	Relative abundance at map-scale	Map-scale features (1:10,000)
Metapelite	Migmatite gneiss	Biotite + **garnet** + sillimanite-migmatite gneiss	30% Bt, 15% Grt 15% Sil, 15% Kfs, 15% Qz, 10% Pl, ± Ilm ± Rt ± Zrc ± Mnz	Gneissic	30	Mappable
		Biotite + garnet + sillimanite ± **cordierite**-migmatite gneiss	30% Bt, 15% Grt, 10% Sil, 15% Kfs, 15% Qz, 10% Pl, 5% Crd, ± Ilm ± Rt ± Zrc ± Mnz	Gneissic	5	Mappable
		Biotite + garnet + sillimanite ± **orthopyroxene**-migmatite gneiss	30% Bt, 15% Grt, 20% Qz, Sil 10%, 10% Kfs, 10% Pl, 5% Opx, ± Ilm ± Rt ± Zrc ± Mnz	Gneissic	3	Mappable
		Fine-grained biotite-migmatite gneiss	15% Qz, 60% Pl, 15% Bt, 10% Grt	Granoblastic-gneissic	/	Metric boudins
	Sillimanite-gneiss	Sillimanite-gneiss	30% Sil, 20% Grt, 15% Bt,15% Pl, 10% Kfs, 10% Qz, ± Gf ± Rt ± Ilm	Foliated	15	Mappable
	Felsic granulite	Felsic granulite	50% Pl, 30% Grt, 10% Bt, 5% Qz, 5% Sil ± Rt ± Zrc	Granoblastic-gneissic	8	Mappable
Metabasite	Amphibolite	Black amphibolite	45% Amp, 25% Pl, 10% Qz, 10 % Cpx, 5% Grt, 5% Bt, ± Ttn	Layered-massive	18	Mappable
		Brown amphibolite	50% Amp, 20% Pl, 20% Cpx, 5% Grt, 5% Bt ± Ilm	Layered-massive	2	Metric boudins
	Granulite	Basic granulite	40% Opx, 30% Pl, 15% Amp, 5% Cpx, 5% Bt, 5% Grt, 5% Qz	Granoblastic-gneissic	2	Metric boudins
Metacarbonate	Marble	Pure marble	100% Cc	Granoblastic	5	Mappable
		Impure marble (Ol + Cpx-marble)	75% Cc, 10% Cpx, 5% Ol, 5% Qz, 5% Phl	Granoblastic-gneissic	5	Mappable
	Calcsilicate-bearing rocks	Calcschists	55% Cc, 20% Qz, 15% Bt, px, 5% Ol, 5%	Foliated	5	Mappable
Dykes and small intrusive body	Granitic-pegmatite	Pegmatite	Qz, Kfs, Pl, Bt, Amp ± Wm	Isotropic holocrystalline	2	Mappable

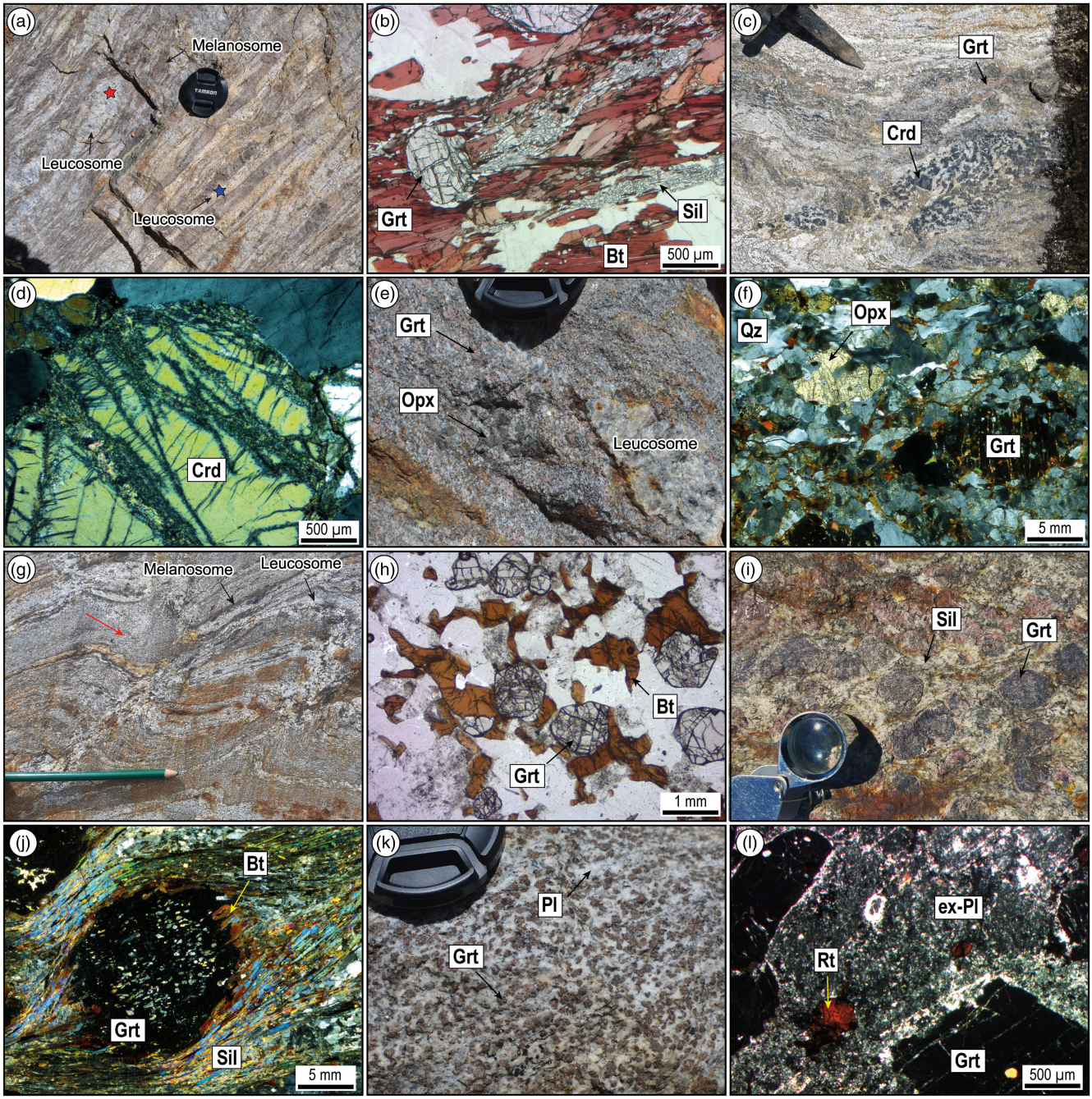

Figure 4. (Colour online) (a) Outcrop of migmatite gneiss with the typical alternation between leucosomes and melanosomes marking the main foliation. The red star indicates the Kfs-bearing leucosome; blue star is the Pl-bearing one. (b) Microscale detail of Bt + Sil foliation in migmatite gneiss (PPL: plane-polarised light). (c) Migmatite gneiss with folded leucosome characterised by the occurrence of dark Crd porphyroblasts (Lac Mort). (d) Crd poprhyroblast in a leucosome of migmatite gneiss substituted by fine-grained Wm along fractures (XPL: crossed-polarised light). (e) Detail of migmatite gneiss with Opx grey blasts and Grt pink blasts (Dzovenno). (f) Microscale view of Opx and Grt porphyroblasts in a migmatite gneiss wrapped by the Bt-rich foliation (XPL). (g) Fine-grained Bt-migmatite gneiss levels cut by thin leucosomes. (h) Millimetric Grt blasts in a fine-grained Bt-migmatite gneiss (PPL). (i, j) Sillimanite-gneiss whose foliation is defined by prismatic sillimanite blasts wrapping around centimetric Grt porphyroblasts (j: XPL). (k) Felsic granulite characterised by widespread presence of plurimillimetric Grt in a white Pl-rich matrix. (l) Microscale detail of Grt porphyroblasts and Pl blasts overgrown by fine-grained white mica in felsic granulite. Rt crystals are also present (XPL).

migmatite gneiss (Fig. 4g). They are abundant at the Lac Mort and Dzovenno areas (Fig. 2). These rocks consist of sub-millimetric quartz, plagioclase, garnet and biotite, the latter defining a weak gneissic fabric whose orientation is parallel to the foliation of the surrounding migmatite gneiss. Locally, their main foliation is crossed by millimetric- to pluricentimetric leucosomes (Fig. 4g). At the microscale, this lithology shows a gneissic to granoblastic structure made of sub-millimetric quartz and plagioclase showing contacts with triple junctions. Garnet constitutes millimetric subhedral blasts with few rounded quartz inclusions. Biotite is mainly interstitial (Fig. 4h) but locally occurs as subhedral to idiomorphic millimetric lamellae defining a weak foliation.

https://doi.org/10.1017/S0016756824000037 Published online by Cambridge University Press

3.a.2. Sillimanite-gneiss

Sillimanite-gneiss occurs as hectometric elongated bodies striking parallel to the axial plane of the isoclinal folds in migmatite gneiss, i.e., with an NE–SW elongation. They are in contact with migmatite gneiss, and locally with black amphibolite and felsic granulite (Fig. 2). At the outcrop scale, the contact of these rocks with migmatite gneiss and felsic granulite can be both sharp and gradual. Sillimanite-gneiss are coarse-grained rocks with a foliated structure consisting of mm-thick layers of plurimillimetric prismatic to locally fibrous sillimanite crystals and minor biotite wrapping around garnet porphyroblasts, the latter with size reaching up to 2 cm in diameter. In this rock type, garnet is characterised by a cm-thick dark-purple core and a millimetre-thick pink rim (Fig. 4i). The sillimanite-rich foliation is pervasive and leucosomes are thinner and discontinuous with respect to those within migmatite gneiss.

At the microscale, the main foliation consists of isoriented idiomorphic prismatic sillimanite (Fig. 4j), along with minor biotite lamellae, and sub-millimetric ilmenite and graphite. Garnet cores are inclusions-rich with fine-grained quartz, graphite and sillimanite inclusions, that locally determine an internal foliation, discordant to the external pervasive foliation of the rock. Conversely, garnet rim is inclusions-poor (i.e., biotite, plagioclase, quartz, sillimanite and rutile). Inclusions within the rim are coarser with respect to those within garnet core and generally have a rounded shape. Locally, a millimetric film made of plagioclase and quartz marks the boundary between garnet crystals and the biotite + sillimanite foliation. Graphite occurs as millimetric to plurimillimetric grains in the cm-sized garnet strain shadows, along with sillimanite.

3.a.3. Felsic granulite

Felsic granulite crops out mainly in the central-southern part of the unit, as metric to decametric bodies interlayered with migmatite gneiss and sillimanite-gneiss and parallel to the strike of the foliation pervasive in migmatite gneiss at the map-scale (Fig. 2). The contact of these rocks with migmatite gneiss and sillimanite-gneiss is mostly gradual. In some outcrops, felsic granulites also occur within the neck of metabasite boudins. At the mesoscale, felsic granulite shows a granoblastic structure made of ~5 mm-sized garnet porphyroblasts surrounded by a white plagioclase-rich matrix (Fig. 4k). Locally, garnet-rich domains highlight a weak layering. Their fabric is locally crosscut by decimetric-thick pegmatitic dykes, made of coarse-grained grey K-feldspars and quartz. At the microscale, garnet is idiomorphic and with sharp edges (Fig. 4l), and rounded sub-millimetric inclusions of quartz, biotite, rutile and minor zircon. Moreover, quartz occurs also as sub-millimetric and irregular films among garnet porphyroblasts. Rutile is particularly abundant in this rock type with respect to other lithologies: it is present as fine-grained inclusions within garnet porphyroblasts or occurs as millimetre-sized blasts in the plagioclase-rich matrix (Fig. 4l). Biotite constitutes deformed millimetric lamellae, in relatively low modal abundance with respect to other metapelites. Sillimanite shows a plurimillimetric prismatic habitus, wrapping around garnet. The plagioclase-rich matrix is often overgrowth by fine-grained aggregates of white mica and epidote (Fig. 4l).

3.b. Metabasite

3.b.1. Basic granulite

Basic granulite is mainly found two localities in the valley (N 45° 55'8" E 7°29'8" and N 45°50'10"; E 7°21'47") as plurimetric to pluricentimetric boudins (not mappable at the 1:10,000 map-scale; Table 1; Fig. 5a) and ellipsoidal lenses elongated parallel to the foliation pervasive in migmatite gneiss, or as close to isoclinally folded layers. These bodies are locally crosscut by a complex network of leucosomes and aplitic or pegmatitic dykes. In the rest of the unit, basic granulite crops out as smaller lenses (from 5 to 10 cm of thickness) within migmatite gneiss, sillimanite-gneiss and felsic granulite, locally separated by biotite + garnet-rich plurimillimetric to pluricentimetric portions (see zoom within Fig. 5a). The internal structure of basic granulite is granoblastic, locally gneissic, characterised by weak isorientation of fine-grained grey-greenish aggregates of pyroxenes and whitish plagioclase blasts. The orientation of their foliation is often discordant with respect to the pervasive foliation in migmatite gneiss. The contact between basic granulite and metapelite is marked by millimetric selvedges made of brown amphibole and biotite. Here, the modal abundance of amphibole gradually increases at the expense of pyroxene, up to becoming an amphibolite. Locally, a centimetric pale greyish amphibole occurs within the amphibole-rich layers, with no preferential orientation (Fig. 5b).

At the microscale orthopyroxene and minor clinopyroxene, orthoamphibole, brown clinoamphibole and minor biotite and quartz are recognised (Fig. 5c): (i) orthopyroxene and clinopyroxene occur as anhedral sub-millimetric blasts; (ii) orthoamphibole is interstitial and colourless with twinning; (iii) plagioclase domains occur as grey to brownish fine-grained aggregates that consist of white mica and epidote (Fig. 5c) and (iv) brown amphibole forms sub-millimetric anhedral crystals growing after pyroxenes. Locally, plurimillimetric garnet porphyroblasts occur in plagioclase-rich domains with a subhedral and locally skeletal habitus including rounded sub-millimetric plagioclase, amphibole and minor quartz showing no preferential orientation.

3.b.2. Brown amphibolite

Brown amphibolite occurs as metric boudins (not mappable at the 1:10,000 map-scale), lenses or folded layers within migmatite gneiss (Table 1; Fig. 5d). These rocks have a fine-grained layered gneissic structure made by the isorientation of brown amphibole and minor plurimillimetric plagioclase aggregates, defining a weak foliation. Pegmatites hosting plagioclase and biotite occur at the contact between these lenses and the surrounding migmatite gneiss or locally crosscutting their fabric.

At the microscale, brown amphibole occurs as subhedral crystals marking the main foliation, together with interstitial sub-millimetric clinopyroxene and orthoamphibole blasts (Fig. 5e). Plagioclase marking the main fabric is replaced by brownish fine-grained aggregates of white mica and epidote. Ilmenite occurs as an accessory phase and marks the main foliation. At the contact of these bodies with pegmatites or leucosomes, clinopyroxene and 'fresh' plagioclase blasts increase in modal abundance together with euhedral biotite, while brown amphibole becomes absent. Locally, plurimillimetric sites made by granoblastic quartz, plagioclase and skeletal garnet similar to those occurring in basic granulites have been detected.

3.b.3. Black amphibolite

These rocks are widespread along the valley as decametric to hectometric bodies, interlayered with metapelites. At the map-scale, these bodies are elongated NE–SW, parallel to the strike of the structures pervasive in metapelites (Fig. 2). Black amphibolite shows a layered structure made by the regular alternance between cm-thick black amphibole-rich and leucocratic pluricentimetric

https://doi.org/10.1017/S0016756824000037 Published online by Cambridge University Press

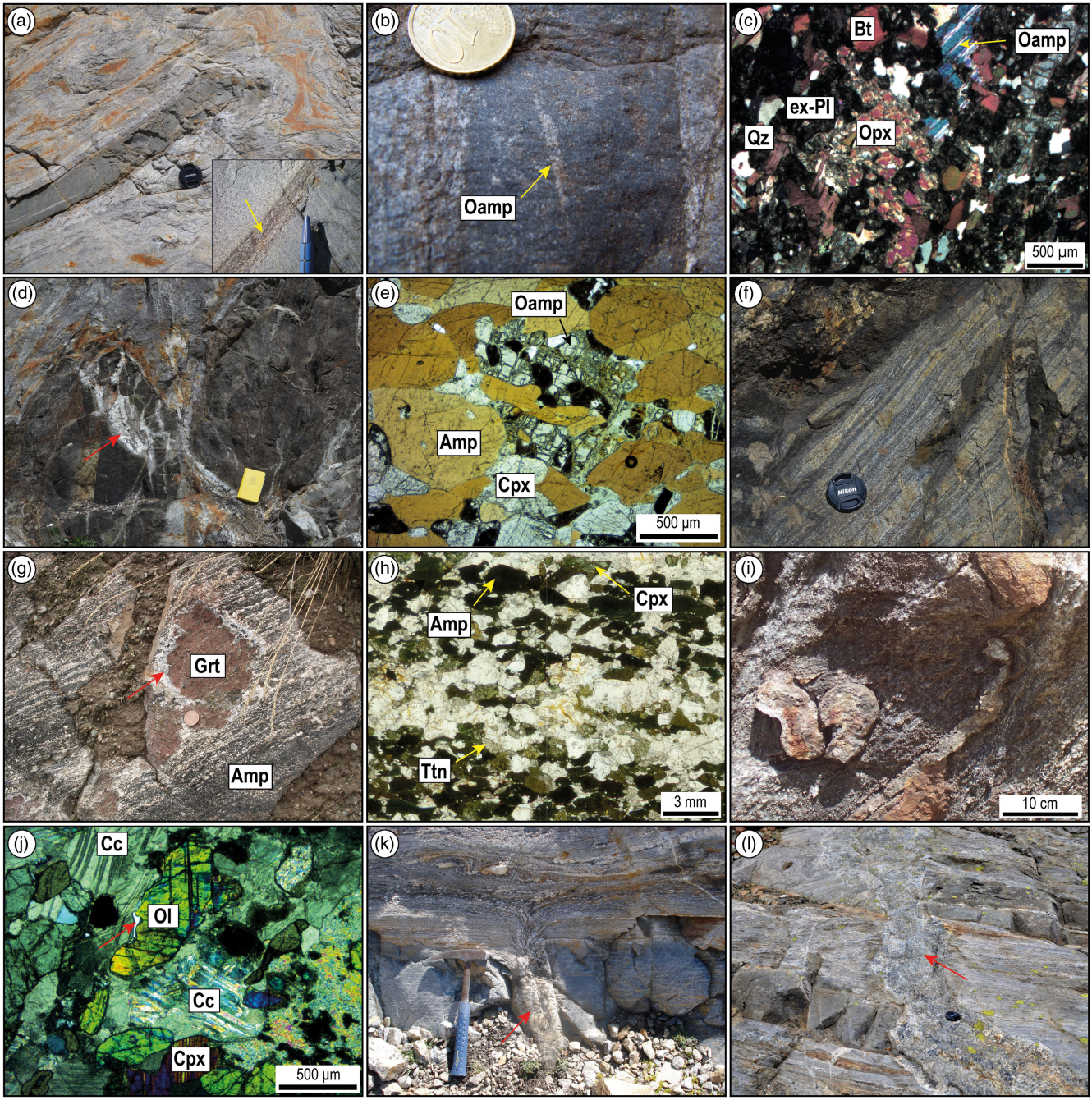

Figure 5. (Colour online) (a) Basic granulite level within migmatite gneiss at the Lac Mort area with a zoom on the selvedge between the level and migmatite on the bottom right. (b) Centimetric Oamp crystal in basic granulite at Thoules. (c) Detail of a basic granulite at the microscale made of granoblastic Opx, retrogressed Pl, Oamp and minor Qz and Bt (XPL). (d) Brown amphibolite boudins cut by Pl–Bt-pegmatite (red arrow) within migmatite gneiss at Oyace. (e) Microscale detail of brown amphibolite (PPL). (f) Black amphibolite outcrop crosscut by a pegmatite dyke. (g) Garnet megablast within black amphibolite surrounded by Pl + Qz-rich aggregates (red arrow). (h) Microscale view of black amphibolite made of Amp + Cpx-rich and Qz + Pl rich-levels (PPL). (i) Outcrop of an impure marble with pluricentimetric Qz-rich disrupted fold hinges. (j) Ol and Cpx blasts in a Cc-rich matrix in impure marble. The red arrow highlights a melt film (XPL). (k) Melt pocket (red arrow) moving from migmatite gneiss and cutting a basic granulite level. (l) Pegmatitic dyke cutting the migmatitic foliation and the basic granulite boudin at Lac Mort area.

plagioclase-rich levels (Fig. 5f and g). Amphibole shape-preferred orientation (SPO) marks the main foliation (i.e., parallel to the regional foliation). Locally, up to 10 – 15 cm in diameter reddish garnet porphyroblasts occur within quartz-feldspathic layers (Fig. 5g). Aggregates of plagioclase, quartz and minor clinopyroxene generally rim these large garnets (Fig. 5g). Clinopyroxene also makes 1–2 cm-thick layers parallel to the main foliation or may occur as coarse-grained aggregates in leucocratic domains, generally wrapped by the main foliation. Locally black amphibolite levels are characterised by a pluricentimetric greenish selvedge at the contact with migmatite gneiss, where amphibole is absent, and pyroxene increases in modal abundance with respect to 'fresh' amphibolites. Leucocratic domains locally crosscut the main foliation of these rocks. Moreover, black amphibolites are crosscut by up to 10 cm-thick Qz+Pl+Amp-pegmatite.

https://doi.org/10.1017/S0016756824000037 Published online by Cambridge University Press

At the microscale amphibole occurs as sub-idiomorphic blasts, marking the main foliation, together with minor sub-millimetric biotite lamellae (Fig. 5h). Clinopyroxene is present both as sub-millimetric relict blasts and as up to cm-thick aggregates in plagioclase and quartz-rich domains. Locally, leucocratic domains are characterised by the presence of a few millimetric calcite blasts. Titanite occurs as an accessory mineral marking the main foliation (Fig. 5h).

3.c. Metacarbonates

This group comprises pure and impure marbles, and minor calcsilicates-bearing rocks (Fig. 5i; Table 1). Metacarbonates at the map-scale occur as decametric to hectometric bodies whose elongation is parallel to the NE–SW strike of the other lithologies (Fig. 2). At the outcrop scale, they occur both as interlayered with metapelites and as metric boudins within migmatite gneiss. Marbles are generally grey and locally yellowish, with a massive structure, which becomes locally gneissic due to the slight isorientation of calcite aggregates or quartz. Locally, greenish millimetric crystals of olivine can be recognised. Calcsilicate-bearing rocks occur mainly in the centre-northern part of the unit; they show a brownish-yellowish colour and are characterised by a foliated structure given by the SPO of calcite aggregates and thin quartz levels. In particular, the latter highlight disrupted fold hinges (Fig. 5i) or occur as up to 20 cm-clasts in the calcite-rich matrix.

At the microscale marble is made of sub-millimetric to millimetric calcite blasts, locally showing large, deformed twinning. Sub-millimetric anhedral olivine and clinopyroxene occur (Fig. 5j). Quartz and plagioclase are locally present together with calcite; plagioclase is overgrown by fine aggregates of white mica. In correspondence with some grain boundaries, thin films made of quartz occur (red arrow in Fig. 5j).

3.d. Aplite and pegmatite

Aplite and pegmatite are widespread throughout the unit and are found in all lithologies, mainly striking NNW–SSE and NW–SE. They form dykes up to 1 m-thick, parallel to the pervasive foliation at the map- and outcrop-scale or cutting the main foliation with complex patterns, made by different crosscutting generations of dykes. In particular, three main types of dykes have been distinguished based on their composition and structure: (i) Qz–Kfs-bearing aplites which occur in m-thick bodies in migmatite gneiss (Fig. 5k and l) and metacarbonate discordant to their main foliation; (ii) Pl–Bt-bearing pegmatite, occurring as 10 cm- to 1 m-thick dykes within brown and black amphibolites, or at the contact between these and migmatite gneiss and (iii) Amp-bearing pegmatites which occur in black amphibolite, cutting their main foliation. The first type forms 5 to 40 cm-thick dykes, with an isotropic structure made of plurimillimetric to centimetric sub-idiomorphic quartz, plagioclase and K-feldspar, plus minor biotite and muscovite. The second type shows an isotropic structure made of pluricentrimetric lamellae of biotite and whitish plagioclase crystals. Amp-bearing pegmatites have an isotropic structure made of dark green plurimillimetric to centimetric idiomorphic crystals in a whitish quartz and plagioclase matrix.

4. Structural analysis

4.a. D_1 stage

The D_1 is well recognisable at the mesoscale in basic granulite and brown amphibolite as an S_1 foliation, which occurs within metre-sized boudins, having various orientations to the main foliation and elongation of main lithological boundaries (Fig. 2). The S_1 foliation has scattered orientations, with three main clusters: at Lac Mort, it dips towards the S, while at Oyace (N 45°51'1" E 7°22'54") toward both W–SW and E (Fig. 2).

In basic granulite, the S_1 foliation is a discontinuous layering marked by the isorientation of pyroxene- and plagioclase-rich domains. At the outcrop scale, the S_1 is geometrically discordant to the long axis of the boudin and to the penetrative foliation that commonly wraps them (Fig. 6a). At the microscale, the S_1 is marked by the weak SPO of Opx I, Bt I (Fig. 7) and minor orthoamphibole. Pl I occurs as granoblastic domains, locally replaced by dark grey fine-grained aggregates.

In brown amphibolite, the S_1 foliation is defined by alternating brown amphibole-rich and plagioclase-rich mm-thick layers, where brown amphibole shows an SPO parallel to the layering (Fig. 6b). Biotite SPO may also contribute to the layering, while clinopyroxene occurs as isolated grains within amphibole-rich layers. At the microscale, Amp I is brown hornblende, and Cpx I occur as interstitial grains in amphibole-rich layers or are associated with Pl I microdomains.

In metapelites, a remnant of this phase is testified by Grt I inclusions-rich cores in bistadial garnets within sillimanite-gneiss. In particular, inclusions of Bt I, Sil I, Qz I and Pl I locally are isoriented marking a foliation discordant to the external one. However, the rounded Bt I, Qz I, Pl I and Sil I inclusions within Grt II and Crd are not always oriented (Fig. 6c and d).

4.b. D_2 stage

During the D_2, the main foliation (S_2) develops, and the main lithological boundaries are parallelised both at map- and mesoscale. The S_2 foliation, the lithological boundaries, and the alignment of basic granulite and brown amphibolite boudins tend to strike NE–SW and dip vertically toward NW or SE (Fig. 2). Sillimanite-gneiss, felsic granulite and black amphibolite bodies interlayered with migmatite gneiss are elongated parallel to the S_2 (Fig. 2). Metre-scale D_2 folds are recognised, folding the S_1 foliation and the lithological boundaries between amphibolite or basic granulite and migmatite gneiss (Fig. 6b). A_2 fold axes are scattered but with two main clusters dipping at a low angle toward the NE and SW. Axial planes (a.p.$_2$) mainly dip toward the S–SE with relatively high dip angles (Fig. 2).

The S_2 is the main foliation in migmatite gneiss and is represented by the alternation between leucosomes and melanosomes (Fig. 6e). In cordierite-bearing migmatite gneiss melanosomes are defined by idiomorphic Bt II, locally in apparent textural equilibrium with Grt II (Fig. 6f), and minor fibrous Sil II. In garnet- and orthopyroxene-migmatite gneiss the S_2 is made by melanosomes whereas biotite has a relict aspect and is deformed. Conversely, in sillimanite-gneiss, the S_2 is almost completely transposed or preserved within microlithons at the microscale. In felsic granulite, the S_2 foliation is marked by the weak isorientation of garnet-rich layers. At the microscale, the S_2 foliation is marked by the SPO of Bt II and minor Sil II in millimetric to plurimillimetric layers, alternating with the leucosomes (Fig. 6f). Grt II, Crd and Opx II porphyroblasts grow in metapelites (Fig. 7). Grt II occurs as inclusions-poor porphyroblasts within migmatite gneiss and sillimanite-gneiss (Fig. 6f), as the rim of inclusions-rich Grt I cores (Fig. 6c), or as blasts in equilibrium with cordierite or orthopyroxene (Opx II). In felsic granulite, the D_2 is testified by the gentle isorientation of Grt II + Pl II domains marking the S_2.

https://doi.org/10.1017/S0016756824000037 Published online by Cambridge University Press

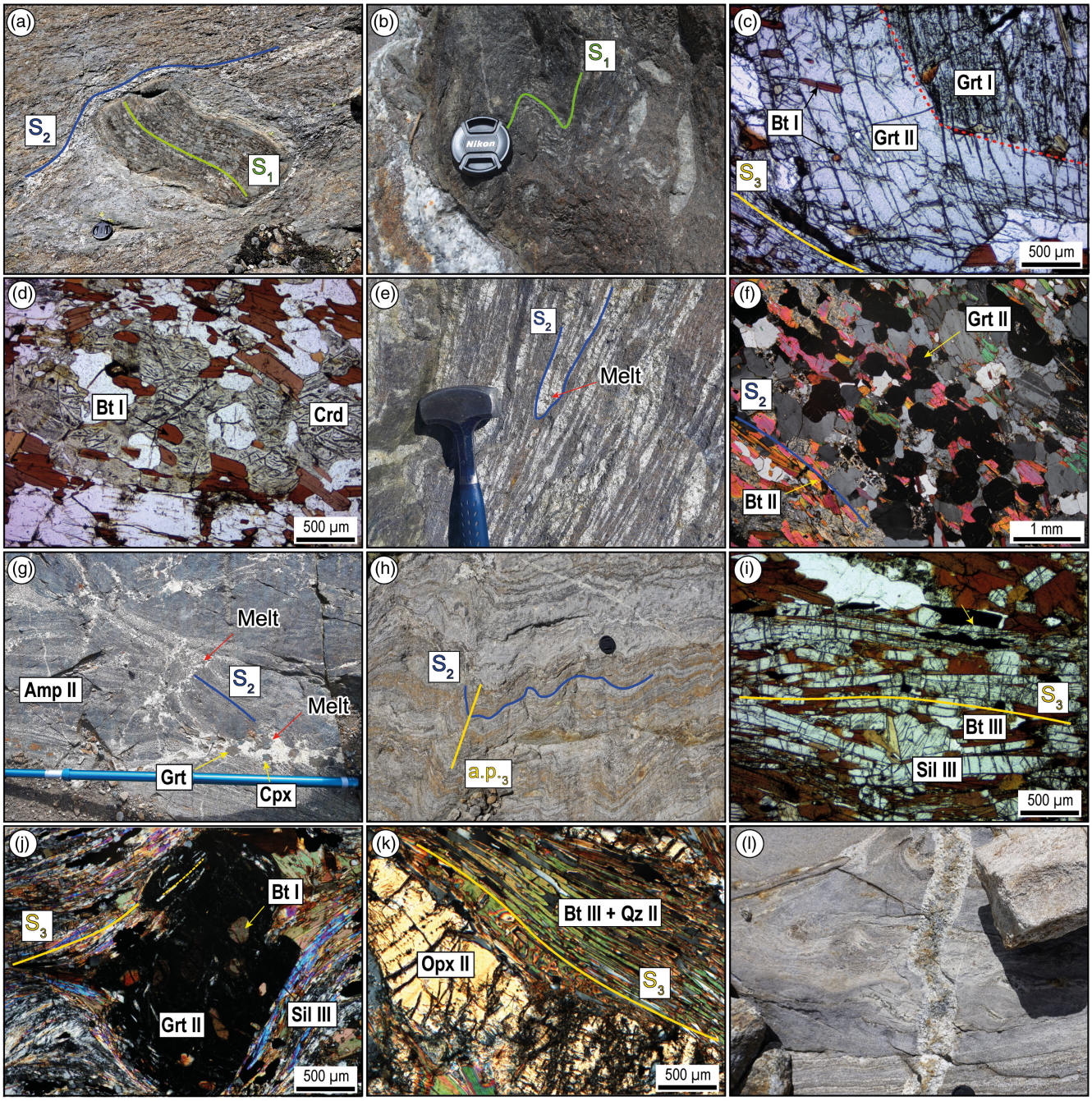

Figure 6. (Colour online) (a) S_1 foliation in basic granulite boudin wrapped by S_2 foliation in migmatites. (b) S_1 folded foliation in brown amphibolite boudin. (c) Inclusions-rich Grt I core rimmed by the inclusions-poor Grt II. The latter includes rounded Bt I and is wrapped by the S_3 foliation (PPL). (d) Rounded Bt I blasts included in Crd in a migmatite gneiss (XPL). (e) S_2 foliation in migmatite gneiss at the Perquis area. f) S_2 foliation in migmatite gneiss at the microscale made by Bt II and Grt II and leucosome (XPL). (g) S_2 foliation in black amphibolite cut by Grt and Cpx-rich leucosomes. (h) S_2 foliation folded at the Lac Mort area. (i) S_3 foliation defined by Sil III + Bt III and locally Ilm in a sillimanite-gneiss (XPL). (j) Syn-kinematic Grt II porphyroblasts with an internal foliation in the rim concordant with the external S_3 (XPL). (k) Opx II blast in migmatite gneiss wrapped by the S_3 foliation made by Bt III + Qz II intergrowths (XPL). (l) Folded pegmatitic dyke intruding migmatite gneiss at the Lac Mort area.

In black amphibolite, the S_2 is made by alternate dark amphibole- plus clinopyroxene-rich and quartz-feldspathic levels (Fig. 6g). The quartz-feldspatic portions of these amphibolites locally show irregular patterns, crosscutting the penetrative S_2 foliation; in these portions, up to 10 cm garnet or pluricentimetric clinopyroxene porphyroblasts occur. At the microscale, the S_2 is marked by the isorientation of the dark Amp II, Cpx II and Pl II + Qz II + Cc in the quartz-feldspathic plurimillimetric to pluricentimetric lithons. S_2 is also locally marked by Ttn blasts.

In marble, the S_2 is marked by the SPO of calcite and quartz-rich aggregates, with minor clinopyroxene or olivine. In calcsilicates, the S_2 foliation is locally mylonitic, wrapping around up to 30 cm quartz-rich porphyroclasts.

https://doi.org/10.1017/S0016756824000037 Published online by Cambridge University Press

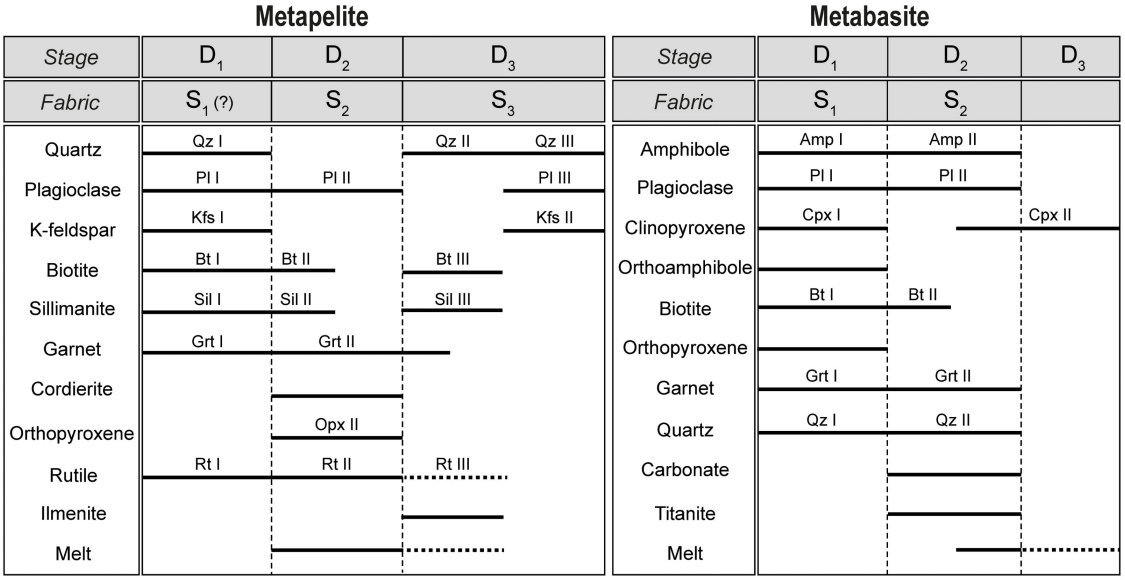

Figure 7. (Colour online) Blastesis-deformation relationships diagrams for metapelite and metabasite relative to the H*T* stages.

During the D_2 stage partial melting of metapelites and, in a minor amount, of black amphibolite occurs. In metapelites, this is mainly testified by the presence of leucosomes rich in quartz and feldspars marking the S_2 foliation. In black amphibolite, it could be testified by the presence of quartz and plagioclase-rich domains, which in some cases, crosscut the main foliation (Fig. 6g).

4.c. D_3 stage

The D_3 deforms the previous S_2 foliation producing tight to isoclinal folds at the meso- and map-scale, with rounded to acute hinges, locally disrupted, leading to the local transposition of the S_2 and the development of S_3 foliation. At the map and mesoscale, the S_3 is pervasive only in the sillimanite-gneiss and is locally parallel to the axial plane of the folds deforming the S_2. It dips mainly towards E–SE and NW with high dip angles. A_3 fold axes plunge mainly towards N–NE and E (Fig. 2).

At the mesoscale, in migmatite gneiss, the D_3 deformation phase is locally testified by close to isoclinal folds that deform the S_2 foliation (Fig. 6h), locally transposed into a S_3, the latter marked by the SPO of Bt III and Sil III. Leucosomes, likely produced during the D_2, occur also within syn-D_3 fold hinges or neck boudins (Fig. 6e). They are made of perfectly igneous granitic texture, but locally the grains show preferred orientation. In sillimanite-gneiss, the S_2 is completely transposed, and the pervasive S_3 is defined by the SPO of Sil III and minor Bt III (Fig. 6i) wrapping around the centimetric Grt I + Grt II porphyroblasts. However, some garnet porphyroblasts show a rim rich in fine sub-millimetric sillimanite inclusions, which outline a foliation concordant and parallel to the external S_3, suggesting that garnet is also syn-kinematic with respect to the D_3 phase (Figs. 6j and 7). At the Lac Mort area, asymmetric folds deform migmatite gneiss, also affecting cordierite blast aggregates. During this stage sillimanite and biotite locally grow after garnet or cordierite. In some cases, fine-grained intergrowths of Bt III + Qz II over Opx II occur (Figs. 6k and 7).

In black amphibolite, the D_3 deformation phase is only locally detectable as close to isoclinal folds deforming the main S_2 foliation.

Aplites and pegmatites intrude all the rock types locally along their main foliation, but in most cases, they crosscut the D_2 and D_3 structures. However, some of the dykes are also folded, probably those emplaced during the late-D_3 stage (Fig. 6l).

4.d. D_4 stage

This stage is localised in some hm-thick belts (Fig. 2) as an S_4 foliation made by white mica and chlorite or as 'coronitic' domains where the blastesis occurs without deformation, better recognisable at the microscale. In metapelites, fine-grained white mica aggregates grow over cordierite along its fractures, or over plagioclase and sillimanite. Chlorite partly pseudomorphs biotite and garnet along fractures. Fine-grained aggregates of epidote and white mica grow after plagioclase both in metabasite and metapelite. Locally, brown amphibole is characterised by a thin rim of green amphibole.

4.e. Inferred stable mineral associations

Based on the relationships between the mineral phases and the observed marking fabrics, it is possible to summarise the inferred mineral associations stable during each deformation phase (Fig. 7).

The D_1 in metapelite is defined by the stable association: Bt I + Sil I + Qz I + Pl I + Kfs I + Grt I ± Rt I.

In basic granulites is defined by Opx I + Cpx I + Qz I + Pl I + Oamp I ± Bt I ± Amp I and by Amp I + Cpx I + Pl I + Qz I ± Bt I ± Oamp I in brown amphibolite.

The D_2 is defined by the stable associations: Grt II + Crd + Opx II + Pl II ± Rt II + melt (in metapelite) or Bt II + Grt II + Crd + Pl II + melt and Amp II + Pl II + Cpx II + Grt II ± Ttn ± melt (in black amphibolite).

https://doi.org/10.1017/S0016756824000037 Published online by Cambridge University Press

The D_3 is characterised by the stable association: Sil III + Bt III ± Qz II ± Rt III ± Ilm ± Gf.

According to microstructural constraints, during the late D_3, the melt produced during the D_2 crystallises (Qz III + Pl III + Kfs II).

5. Whole-rock chemistry

5.a. Metapelite

Metapelites show mineralogical differences confirmed by whole-rock chemical variations. In particular, SiO_2 in migmatite gneiss covers a relatively wide range of values from ~42 to 75 wt%, while in sillimanite-gneiss this range is smaller, i.e., from ~46 to 60 wt% (Fig. 8). Felsic granulite shows a SiO_2 content of ~43 wt%, similar to sillimanite-gneiss (Fig. 8). Alkali content is similar among all analysed metapelites, between ~3 and ~6%, except for some modal-derived bulk compositions having relatively low values (<2%) or higher, up to ~8% (Fig. 8a). Al_2O_3 wt% has highest values in correspondence of sillimanite-gneiss, while decreases in most of the migmatite gneiss samples (Fig. 8b). Pegmatite has a relatively low concentration of Al_2O_3 and a higher one of SiO_2 of ~72 wt% (Fig. 8b). The iron content (Fe_2O_3 wt%) of migmatite gneiss varies between ~3 and 20 wt%, depending on garnet modal abundance; in sillimanite-gneiss, it ranges from ~7 to 14 wt% (Fig. 8c). Pegmatite has the lowest iron content (~2%). The MgO and CaO (wt%) contents are constant through different samples: they range from ~1 to 7 wt% (Fig. 8d) and ~0.1% to ~5% (Fig. 8e), respectively. A distinction between migmatite and sillimanite-gneiss is evident from the TiO_2 values: it is lower in migmatite gneiss in which it ranges between ~0.1 and 2%, while is higher in sillimanite-gneiss (~1.4 to 3 wt%; Fig. 8f).

5.b. Metabasite

Whole-rock analyses on metabasites confirm the differences among the described groups: black amphibolite shows a SiO_2 wt% content ranging between ~40 and 47%, while brown amphibolite at 45 wt%; basic granulites show higher values, ranging from ~45 to 55 wt% (Fig. 8). The alkali content varies between ~1 and 6.8 wt%, with the lowest values in basic granulite samples from Nicot (1977). Al_2O_3 ranges between ~4 and 22% in all metabasites (Fig. 8b). Fe_2O_3 wt% content is higher in black amphibolite (~13 – 20 wt%) and lower in brown amphibolite (~12%) and basic granulite (~7 – 15%; Fig. 8c). MgO content is between ~4.8 and 7 wt% in most of the metabasites, with higher values (up to ~17%; Fig. 8d) in brown amphibolite and two samples of basic granulite. The difference among metabasite is evident also looking at the CaO content: the highest values are in correspondence with black amphibolite and brown amphibolite (up to 11 wt%) and decrease in basic granulite (Fig. 8e). TiO_2 ranges between ~0.4 and 6%, with the highest values in black amphibolite (Fig. 8f).

6. Mineral chemistry

According to the microstructural relationships described above, mineral phases were selected for chemical analyses performed by the electron microprobe analyser. In this section, mineral chemistry is described and discussed with respect to the bulk rock system. All data from this work and Nicot (1977) are in Appendixes 1–5 in the Supplementary Material available online.

Biotite composition in metapelites varies depending on the lithotype, mostly between Grt-only metapelite (i.e., sillimanite-gneiss and migmatite gneiss), and cordierite- and orthopyroxene-bearing migmatite gneiss, but without a clear distinction between biotite formed during different stages (i.e., between Bt I, Bt II and Bt III distinguished from their microstructural position; Fig. 9a). The lowest Ti a.p.f.u. (atoms per formula units) values correspond to biotites from Bt+Grt+Sil±Crd-migmatite gneiss, which are characterised by Ti contents from 0.27 to 0.69, with most of the biotite having Ti content in the 0.35–0.60 range and an average of 0.44 ($1\sigma = 0.09$). Biotite from Bt+Grt+Sil-migmatite gneiss has Ti ranging between ~0.35 and 0.65 a.p.f.u. and has slightly higher average values (0.47, $1\sigma = 0.08$). Biotite from Bt+Grt+Sil±Opx-migmatite has the highest content in Ti, between 0.55 and 0.79. Ti values of biotite from sillimanite-gneiss range between 0.20 and 0.70, but with two clusters at 0.25–0.45 and 0.4–0.7, depending on the sample. The Ti a.p.f.u. content values in biotite from felsic granulite are scattered and range between ~0.30 and 0.65. Ti values in biotite from fine-grained Bt-migmatite gneiss range between ~0.35 and 0.65, with an average of 0.49 a.p.f.u. for the felsic granulites and 0.42 for the gneiss (Fig. 9a). The X_{Mg} varies between 0.50 and 0.72 in Bt+Grt+Sil±Crd-migmatite gneiss and between 0.57 and 0.66 in the Bt+Grt+Sil±Opx-migmatite gneiss. In Bt+Grt+Sil-migmatite gneiss there are two clusters, the first one has X_{Mg} between ~0.40 and 0.55 and the second has values in the 0.53 and 0.77 range. Biotite in sillimanite-gneiss has X_{Mg} between 0.57 and 0.77, while in felsic granulite, it is 0.68–0.70 (Fig. 9a). X_{Mg} in biotite from fine-grained Bt-migmatite gneiss range between 0.55 and 0.63 (Fig. 9a).

Biotite from black amphibolite has Ti between 0.34 and 0.40 a.p.f.u., and X_{Mg} of 0.46 and 0.47. In brown amphibolite there are two main clusters: (i) Ti values between 0.53 and 0.66 a.p.f.u. and X_{Mg} from 0.54 to 0.65; (ii) Ti a.p.f.u. from 0.35 to 0.38 and X_{Mg} 0.79–0.80. The former is in correspondence with biotite marking the S_1 foliation, the latter is in correspondence with biotite growing at the boundary with the leucosome of surrounding metapelite (Fig. 9b).

Garnet from all metapelites is Fe-rich, with FeO wt% greater than 30. Generally, single garnet crystals are relatively chemically homogeneous grains, with only local zoning toward the rim, especially in contact with biotite. Zoning is more pronounced in sillimanite-gneiss where it is possible to distinguish a garnet core and garnet rim. In detail, garnet from Bt+Grt+Sil-migmatite gneiss has almandine content (Alm) ranging from ~65 to ~80% and pyrope (Prp) between 15 and 30%. Garnets from Bt+Grt+Sil±Crd-migmatite gneiss show Alm content of ~65–76%; Prp from 20 to 30% and grossular (Grs) and spessartine (Sps) are ~2–3% and ~1–3% respectively. Garnets from Bt+Grt+Sil ±Opx-migmatite gneiss are more homogeneous (Alm ~60 and 65%) and are higher in CaO, with Grs from 6 to 11% (Fig. 9c). Garnet in fine-grained Bt-migmatite gneiss has Alm content between 70 and 75% and Prp from 20 to 26%; Grs and Sps are constant at ~20% (Fig. 9c). In sillimanite-gneiss, there is an increase in the Fe content and Mg decrease from Grt I (cores) to Grt II (rims), with Alm content varying from core to rim from ~60 to ~80%, and Prp content increasing from ~15 to ~35%. Grs and Sps range between 5–7% and 1–2%, respectively (Fig. 9c). Felsic granulite garnets are also relatively homogeneous: the Alm content is between ~59–69% while the Prp content is between ~29–34%; Grs and Sps are 5–8% and 1–2% respectively (Fig. 9c). Garnet analyses from metabasite have been taken from Nicot (1977). Garnets from black amphibolite are Alm-rich, but relatively enriched in the Grs component with respect to metapelite. Alm content ranges from ~62 to 77%, while Prp content varies only

https://doi.org/10.1017/S0016756824000037 Published online by Cambridge University Press

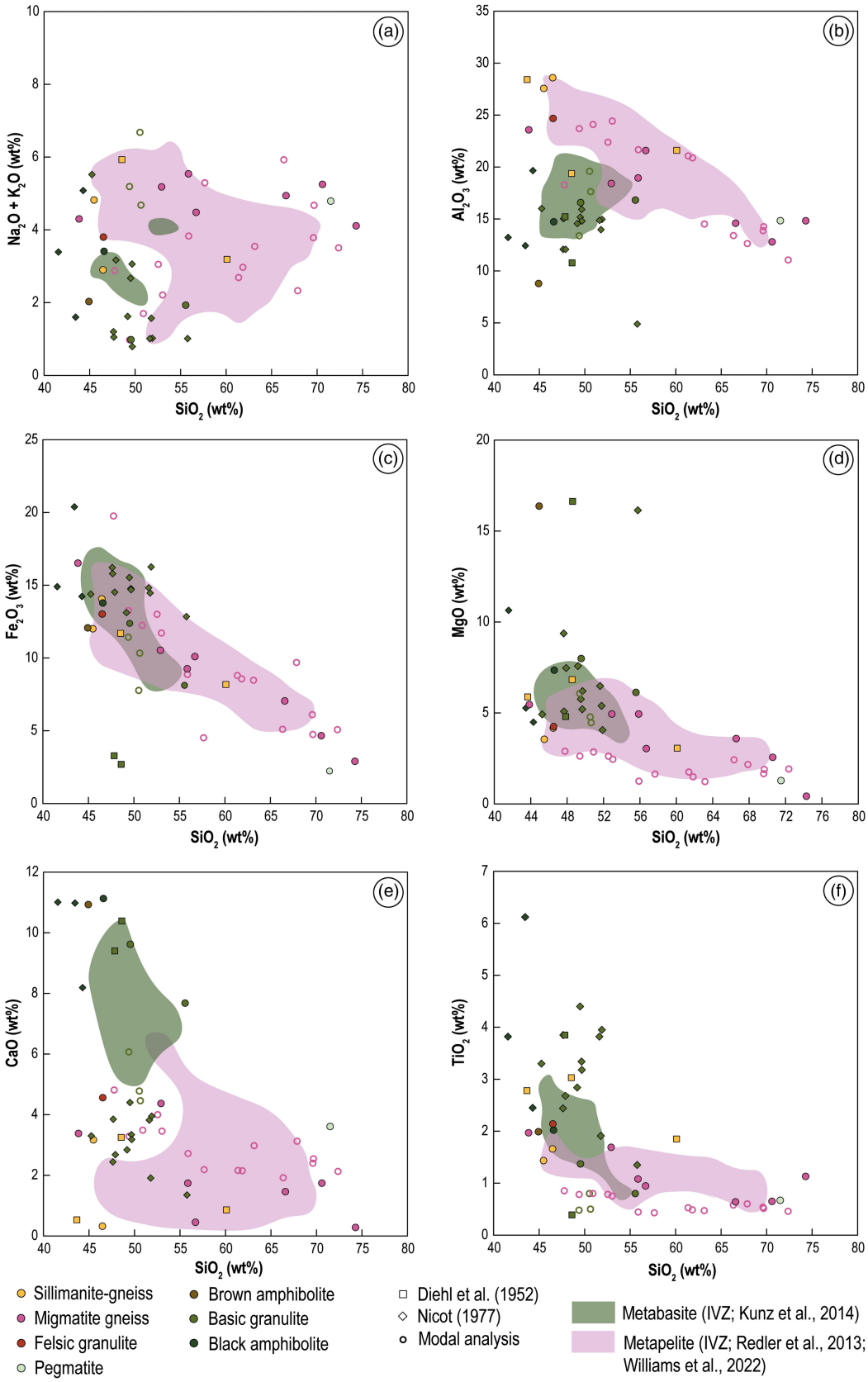

Figure 8. (Colour online) Whole-rock compositions of the main rock types of the VP with shaded areas indicating data from the literature of IVZ (Kunz *et al.* 2014; Redler *et al.* 2013; Williams *et al.* 2022). (a) SiO_2 vs. alkali content plot. (b) SiO_2 vs. Al_2O_3 wt% in metapelite. (c) SiO_2 vs. FeO + Fe_2O_3 wt% plot. (d) SiO_2 vs. MgO wt% plot. (e) SiO_2 vs. CaO wt% plot. (f) SiO_2 vs. TiO_2 wt% plot.

https://doi.org/10.1017/S0016756824000037 Published online by Cambridge University Press

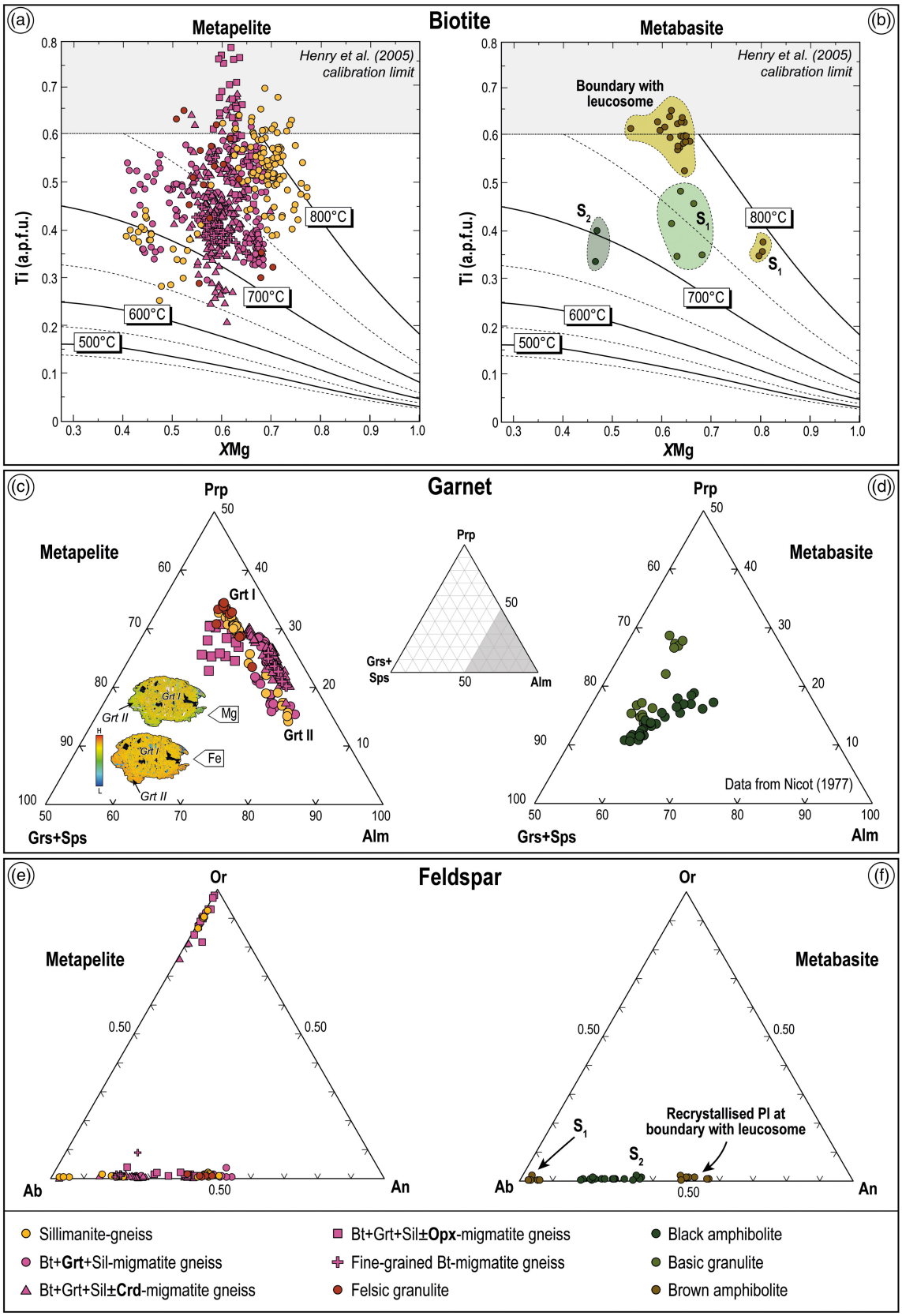

Figure 9. (Colour online) (a, b) X_{Mg} (Mg/Mg+Fe) vs Ti (a.p.f.u.) content in biotite (22 oxigens) from metapelite and metabasite (isolines are after Henry *et al.* 2005). (c, d) Garnet ternary plot of metapelite (with Mg and Fe X-Ray maps) and metabasite (data from Nicot, 1977). (e, f) Feldspar ternary plots of metapelite and metabasite.

https://doi.org/10.1017/S0016756824000037 Published online by Cambridge University Press

between ~24 and 26%. Basic granulite garnets show two clusters of composition: one is richer in the Prp component, and one is richer in the Alm and Grs+Sps components (Fig. 9d).

Feldspars from Bt+Grt+Sil-migmatite correspond to K-feldspar and plagioclase: the former has Or (orthoclase) component ranging from 0.87 to 0.92, the latter has An component ranging between 0.25 and 0.54. Plagioclase in Bt+Grt+Sil±Crd-migmatite gneiss varies from pure Ab crystals to having An (anorthite component) between 0.20 and 0.42. K-feldspar has Or content ranging from 0.76 and 0.81 (Fig. 9e).

Bt+Grt+Sil±Opx-migmatite gneiss plagioclase has An component ranging from 0.20 to 0.43; K-feldspar has Or component ranging between ~0.80 and 0.90. In sillimanite-gneiss, they have two clusters: one has An of 0.46, and the other is richer in Ab and has lower An content (0.03–0.20). K-feldspars have Or content of ~0.90 (Fig. 9e). Feldspar from felsic granulite corresponds only to plagioclase. An values are between ~0.40 and 0.50 (Fig. 9e). Plagioclase from black amphibolite, marking the S_2 foliation, has An content ranging from ~0.18 to 0.35. Those from brown amphibolite show two clusters of compositions: one is almost Ab-pure and corresponds to plagioclase marking the S_1 foliation, and the second has An ranging between 0.50 and 0.56 corresponding to recrystallised plagioclases at the boundary with metapelite leucosome (Fig. 9f).

Amphibole from black amphibolite, considering both our new data and those from Nicot (1977), has Ca content approximately of 1.7 a.p.f.u. Fe_{TOT} + Mg a.p.f.u. content is 4.1–4.4 a.p.f.u (Fig. 10a). Al_{TOT} varies between ~1.7 and 2.7 a.p.f.u. while the Ti content ranges between 0.15 and 0.26 a.p.f.u (Fig. 10b). Amphibole from brown amphibolite has Ca content varying between 1.41 and 1.89 a.p.f.u. Fe_{TOT} + Mg a.p.f.u. range from 4.1 to 4.6 (Fig. 10a). Al_{TOT} ranges from 1.7 to 2 (Fig. 10b). Amphiboles from black amphibolite correspond to pargasite, those from brown amphibolite correspond to Mg-hornblende and minor pargasite. Most of the amphiboles in basic granulite have almost no Ca, and correspond to orthoamphibole, apart from a few grains having Ca of ~1.8 a.p.f.u. Fe^{2+} in orthoamphibole is of ~2.4 a.p.f.u. while in the Ca-rich one is ~0.9 a.p.f.u. (Fig. 10a). Orthoamphibole has Al_{TOT} and Ti relatively low compared to clinoamphibole from other lithologies (Fig. 10b).

Pyroxene in migmatite gneiss is enstatite (Fig. 10c and d). Fe is 0.8 a.p.f.u., Mg is 1.16 a.p.f.u. In black amphibolite, clinopyroxene is diopside (Fig. 10d), with low Fe^{2+} and Mg contents. Fe ranges between 0.22 and 0.52 a.p.f.u., while Mg ranges from 0.58 to 0.74 a.p.f.u. (Fig. 10c). Al varies between 0.07 and 0.41 a.p.f.u. while Na ranges from 0.05 to 0.13 a.p.f.u. Brown amphibolite has both clino- and orthopyroxene. The former corresponds to those with relatively low Fe^{2+} and Mg a.p.f.u. values (Fig. 10c) and the latter to those with higher values. Both clino- and orthopyroxenes mark the S_1 foliation. Al varies between 0.03 and 0.11 while Na reaches 0.03 a.p.f.u. Pyroxenes from basic granulite correspond to orthopyroxene, with relatively high Fe^{2+} and Mg a.p.f.u. values of ~0.75 and ~1.20, respectively (Fig. 10c). They fall in the compositional range of enstatite (Fig. 10d).

Cordierite from migmatite gneiss shows a slight chemical zoning: X_{Mg} (Mg/Mg+Fe) varies from 0.65 to 0.77, i.e., from the core towards the rim. Fe^{2+} a.p.f.u. values range from 0.45 to 0.71, while Mg varies between 1.30 and 1.53 a.p.f.u. (Fig. 10e).

Rutile in sillimanite-gneiss has Nb concentrations covering a wide range of values from ~200 to ~2600 ppm and Zr concentrations from ~400 up to ~2000 ppm. Cr concentrations vary between ~200 and ~700 ppm. Rutiles from Bt+Grt+Sil-migmatite gneiss are more homogeneous than those from sillimanite-gneiss. Nb varies from ~800 to ~1600 ppm (except for one grain which has 2500 ppm of Nb) and Zr from ~440 to ~1400 ppm (Fig. 10f). Cr concentrations range from ~250 to ~450 ppm (Fig. 10f). Rutiles of felsic granulite have Fe concentration ranging between ~1000 and 6000 ppm but with a main cluster between ~1000 and 2000 ppm. Zr content ranges between ~500 and 2500 ppm. Nb concentration is between ~100 and 2000 ppm, while Cr is quite constant at about 600 ppm with a maximum of ~1600 ppm.

7. Temperature estimations

7.a. Grt–Bt exchange

The Grt–Bt exchange between garnet and biotite has been applied on three metapelite samples, on a total of 20 pairs. For these pairs have been used both analyses from garnet core and included biotite, or garnet rim and neighbouring biotite in the matrix or in garnet strain shadows. The Ferry and Spear (1978) calibration has been chosen since garnet is mainly Fe- and Mg-rich. Sillimanite-gneiss shows temperatures ranging from 662 to 736 °C, from three pairs. Bt+Grt+Sil±Crd-migmatite gneiss has temperatures ranging from 556 to 730 °C while those from Bt+Grt+Sil±Opx-migmatite gneiss, taken from four pairs are between 680 and 770 °C (Fig. 11a; Table 2).

7.b. Zr-in-rutile

The temperature of rutile crystallisation has been calculated based on its Zr content following the calibration of Tomkins *et al.* (2007). Since the Zr-in-rutile thermometer is pressure-dependent, a value of 0.7 GPa has been used for the calculations. This pressure was estimated for the migmatitic events by Manzotti and Zucali (2013) and Gardien *et al.* (1994) based on conventional geobarometry. A total of 203 results have been obtained: 112 from sillimanite-gneiss, 43 from Bt+Grt+Sil-migmatite gneiss, and 48 from felsic granulite. Sillimanite-gneiss yielded temperatures ranging from 691 to 818 °C (see Table 2 for average *T* °C and errors), while Bt+Sil+Grt-migmatite gneiss temperatures vary between 683 and 773 °C (Figs. 11b and 12; Table 2). In felsic granulite, temperatures range between 667 and 843 °C (Fig. 11b).

7.c. Ti-in-biotite

The Ti-in-Bt thermometer (Henry *et al.* 2005) has been applied to biotites from three different microstructural domains (Bt I, Bt II and Bt III) on 18 samples (Fig. 11c). Four samples of sillimanite-gneiss collected at different localities have been analysed (139 biotite analyses used). Except for one sample (belonging to the west of Vessonaz stream) having temperatures between 649 and 727 °C, sillimanite-gneiss have values between 721 and 812 °C (see Table 2 for average *T* °C for each sample and error). Five samples of Bt+Grt+Sil-migmatite gneiss have been analysed (167 biotite analyses used) giving temperatures between 676 and 784 °C. Five Bt+Grt+Sil±Crd-migmatite gneiss samples (179 biotite analyses used) have temperatures ranging from 654 to 789 °C. Temperatures in Bt+Grt+Sil±Opx-migmatite gneiss (27 biotite analyses used) are quite higher: the two samples have temperatures ranging from 700 to

https://doi.org/10.1017/S0016756824000037 Published online by Cambridge University Press

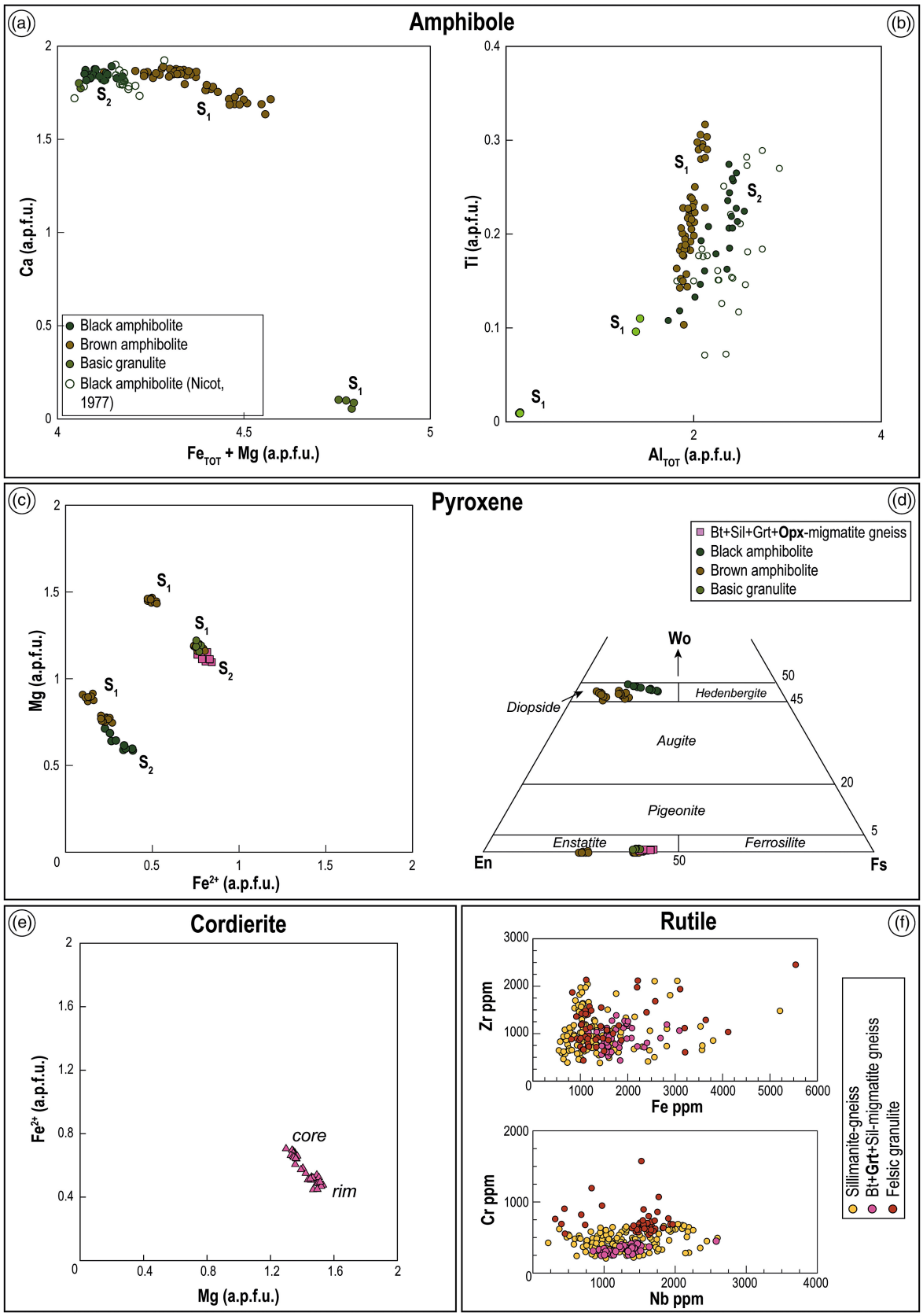

Figure 10. (Colour online) (a) Fe_{TOT} + Mg (a.p.f.u.) vs Ca (a.p.f.u.) plot of amphiboles from metabasite. (b) Al_{TOT} vs Ti (a.p.f.u.) plot of amphibole of metabasite. (c) Fe^{2+} vs Mg (a.p.f.u.) content plot of pyroxene from both migmatite gneiss and metabasite. (d) Ternary compositional diagram showing pyroxene variation in the terms of Fe, Mg and Ca of both migmatite gneiss and metabasite. (e) Mg (a.p.f.u.) vs Fe^{2+} (a.p.f.u.) in cordierite from migmatite gneiss. (f) Compositional variations diagram of rutile from metapelites: on the top Fe vs Zr ppm plot, at the bottom Nb vs Cr ppm plot.

https://doi.org/10.1017/S0016756824000037 Published online by Cambridge University Press

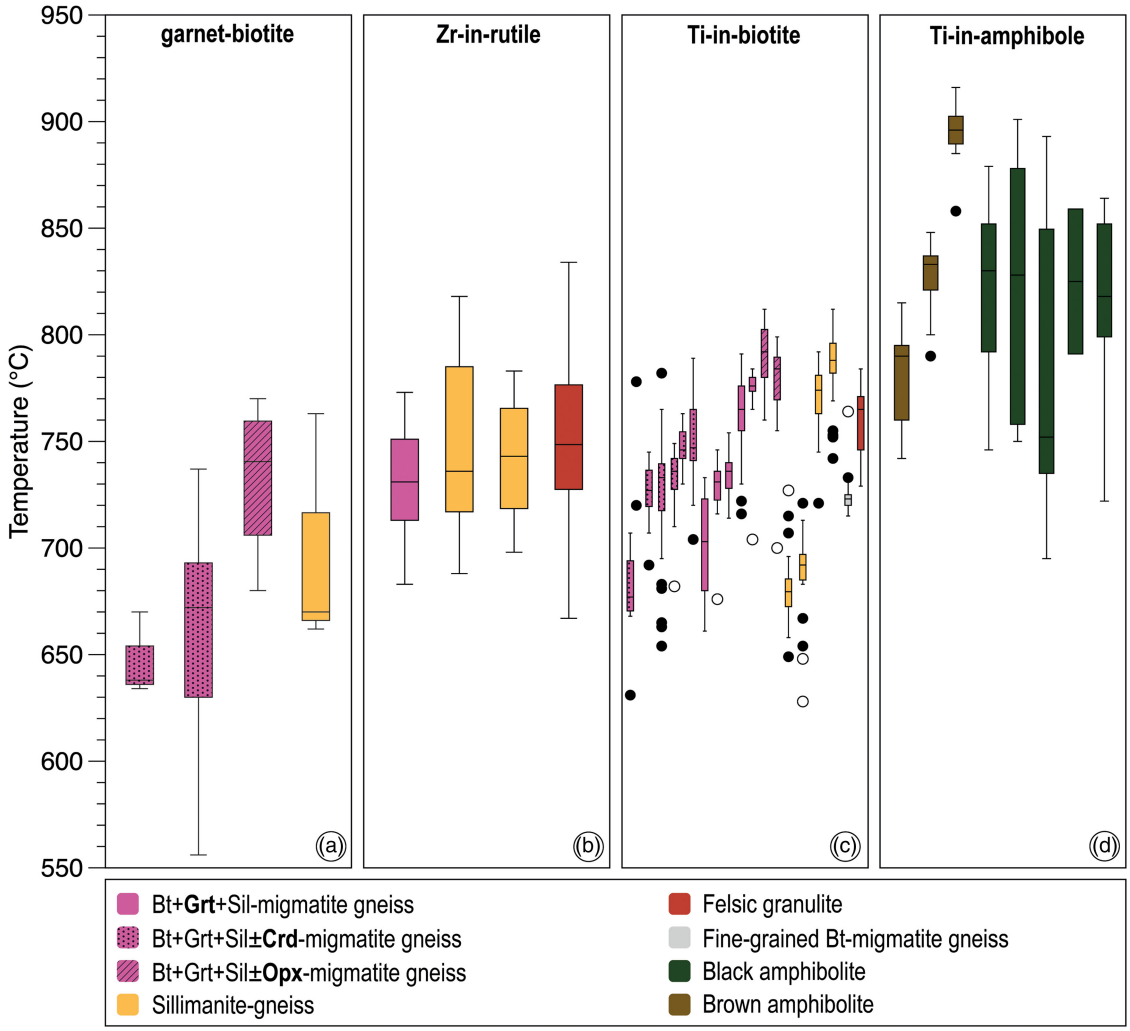

Figure 11. (Colour online) Summary of the *T* °C ranges of each analysed sample for different applied methods. (a) garnet-biotite thermometer (Ferry & Spear, 1978). (b) Zr-in-rutile thermometer of Tomkins *et al.* (2007). (c) Ti-in-biotite thermometer of Henry *et al.* (2005). (d) Ti-in-amphibole thermometer of Liao *et al.* (2021).

799 °C and from 760 to 812 °C pointing to higher average *T* °C (Table 2). Fine-grained Bt-migmatite gneiss (25 analyses used) yielded temperatures between 715 and 764 °C. Biotite from felsic granulite has been analysed only on one sample (from the Perquis area) due to its low modal abundance. Temperatures (13 biotite analyses used) are from 729 to 784 °C (Table 2). Since the chemical composition between different biotite generations is similar, the resulting temperatures do not show significant variations (Fig. 12).

7.d. Ti in-amphibole

The Ti-in-Amp calibration of Liao *et al.* (2021) has been used on 34 analyses of black amphibolite (plus 18 analyses from Nicot, 1977) and 51 analyses of brown amphibolite (Fig. 11d). Black amphibolite has temperatures ranging from 746 to 880 °C with two main clusters at 767 ± 19 °C and 844 ± 21 °C (Figs. 11d and 12; Table 2). Brown amphibolite has relatively higher temperatures ranging from 858 to 916 °C (Figs. 11d and 12; Table 2). Among the Nicot (1977) samples, D48 gave temperatures between 791 and 859 °C with a mean of 825 ± 48 °C; D16 gave temperatures between 695 and 893 °C with a mean of 783 ± 74 °C. B78 gives temperatures ranging between 750 and 901 °C with a mean value of 823 ± 68 °C (Figs. 11d and 12; Table 2).

8. Pressure estimations

Pressures have been obtained applying two geobarometers, i.e., the Grt–Crd barometer (Bhattacharya, 1986) on one cordierite-bearing sample and the Pl–Amp barometer (Molina *et al.* 2015) on one black amphibolite sample.

8.a. Grt–Crd geobarometer

The Grt–Crd barometer (Bhattacharya, 1986) has been used on the 33SC sample, corresponding to a Bt+Sil+Grt±Crd-migmatite gneiss. Three pairs of Grt–Crd (using cordierite rim and core, without significant *P* differences) have been used for the calculation, both with the minimum and maximum *T* °C estimated through the Ti-in-Bt thermometer on the same sample (i.e., 704 and 769 °C, respectively). Both temperatures used yielded similar values, ranging between 0.55 and 0.58 GPa, with an error of 0.01 GPa.

https://doi.org/10.1017/S0016756824000037 Published online by Cambridge University Press

Table 2. *T* °C estimated for different samples with the standard deviation reported.

Sample	Lithology	*T* °C [1]	*T* °C [2]	*T* °C [3]	*T* °C [4]	Locality
MM15	Sillimanite-gneiss	–	787 ± 14	–	–	Localitè Collatte
P55	Bt+Grt+Sil-migmatite gneiss	–	735 ± 9	–	–	Thoules
P74	Bt+Grt+Sil-migmatite gneiss	–	764 ± 17	–	–	Thoules
P72B	Brown amphibolite	–	–	–	894 ± 15	Thoules
AS488	Brown amphibolite	–	–	–	827 ± 16	Oyace
AS584	Sillimanite-gneiss	742 ± 27	772 ± 16	698 ± 56	–	Perquis
AS583	Sillimanite-gneiss	746 ± 38	–	–	–	Perquis
AS582B	Bt+Grt+Sil-migmatite	732 ± 23	773 ± 16	–	–	Perquis
FC12	Felsic granulite	–	760 ± 18	–	–	Perquis
AS587	Black amphibolite	–	–	–	[1]767 ± 19 [2]844 ± 21	Perquis
B101 (N)	Black amphibolite	–	–	–	748 ± 17	Perquis
B78 (N)	Black amphibolite	–	–	–	823 ± 68	Perquis
VP34	Bt+Grt+Sil±Crd-migmatite gneiss	–	726 ± 26	–	–	Vessonaz stream
33SC	Bt+Grt+Sil±Crd-migmatite gneiss	–	*751 ± 16	664 ± 54	–	Vessonaz stream
34SC	Sillimanite-gneiss	–	680 ± 16	–	–	Vessonaz stream
VP38	Felsic granulite	751 ± 37	–	–	–	Vessonaz stream
CP-T2	Bt+Grt+Sil±Opx-migmatite gneiss	–	774 ± 28	–	–	Dzovenno
CP-B1	Bt+Grt+Sil±Opx-migmatite gneiss	–	790 ± 13	733 ± 38	–	Dzovenno
DB9	Black amphibolite	–	–	–	[1]733 ± 12 [2]812 ± 9 [3]858 ± 6	Dzovenno
D48 (N)	Black amphibolite	–	–	–	825 ± 48	Dzovenno
D16 (N)	Black amphibolite	–	–	–	783 ± 74	Dzovenno
I51	Sillimanite-gneiss	–	689 ± 21	–	–	Lac Place Moulin
I_22_07	Bt+Grt+Sil±Crd-migmatite gneiss	–	730 ± 19	647 ± 20	–	Lac Place Moulin
CBP8	Bt+Grt+Sil-migmatite gneiss	–	729 ± 13	–	–	Lac d'Orein
CBP10	Bt+Grt+Sil±Crd-migmatite gneiss	–	679 ± 20	–	–	Lac d'Orein
CBP7	Bt+Grt+Sil-migmatite gneiss	–	700 ± 24	–	–	Gran Place
31SC	Bt+Grt+Sil±Crd-migmatite gneiss	–	726 ± 15	–	–	Lac Mort
6CP	Bt+Grt+Sil±Crd-migmatite gneiss	–	747 ± 12	–	–	Lac Mort
FC2	Fine-grained Bt-migmatite gneiss	–	724 ± 10	–	–	Lac Mort
2CP	Brown amphibolite	–	–	–	[1]753 ± 10 [2]796 ± 10	Lac Mort

[1]Zr-in-Rt of Tomkins *et al.* (2007);
[2]Ti-in-Bt of Henry *et al.* (2005);
[3]Grt–Bt of Ferry and Spear (1978);
[4]Ti-in-Amp of Liao *et al.* (2021). N are samples from Nicot, (1977);
*is the value from Caso (2023).

8.b. Pl–Amp geobarometer

The Pl–Amp geobarometer of Molina *et al.* (2015) has been used on a total of 17 pairs. Even for this sample, we used both the minimum and maximum *T* (i.e., 767 and 879 °C) for the *P* estimation, which was calculated through the Ti-in-Amp thermometer. Obtained pressure ranges between 0.8 ± 0.08 GPa (at 767 °C) and 1.1 ± 0.10 GPa (at 879 °C).

9. Discussions

The VP is well suited to investigate: (i) pervasive fabrics at unit scale during melt production and migmatisation; (ii) the thermal state of the lower crust during the melt-producing and melt-consuming stages and (iii) the tectono-metamorphic evolution of the Adria lower crust and its geodynamic significance, comparing the VP with the well-studied case of the IVZ.

9.a. Pervasive fabrics associated with melt production and migmatisation at the unit scale

Differently to previous studies, which were merely lithological (i.e., Diehl *et al.* 1952; the Monte Cervino Sheet n.70 of Geological Map of Italy; Dal Piaz *et al.* 2016) or restricted to more localised areas (Manzotti & Zucali, 2013), this work extends the description of rock types and associated structures at the whole unit scale.

https://doi.org/10.1017/S0016756824000037 Published online by Cambridge University Press

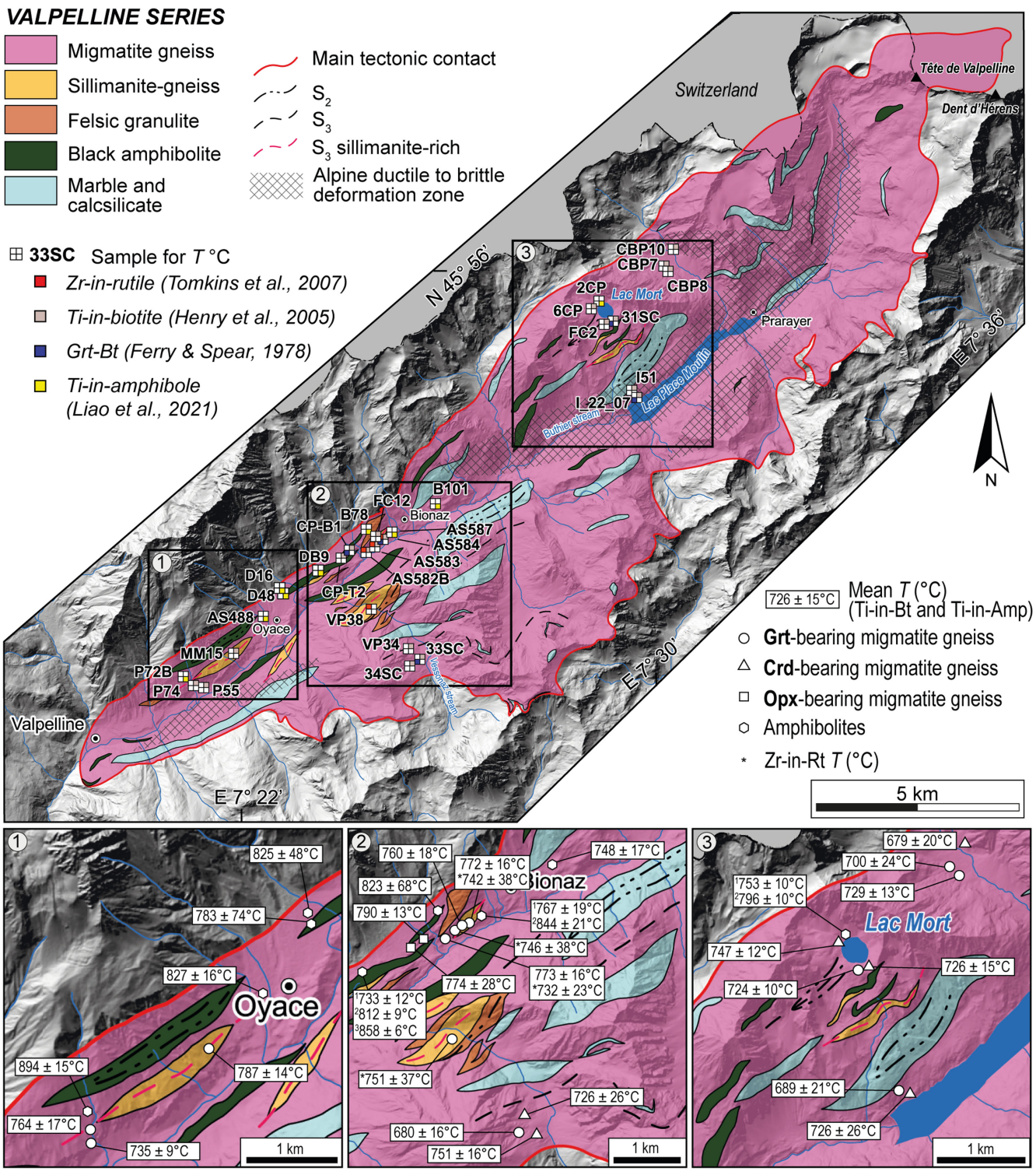

Figure 12. (Colour online) Geological sketch map of the VP with the position of samples analysed for temperature estimations and zoom with the mean temperatures and errors reported.

This work detailed the distribution of partially melted metapelites with variable textures and %vol of leucosomes, with decreasing melt abundance: migmatite gneiss, sillimanite-gneiss and felsic granulite. Metabasites have also been thoroughly described and separated in terms of bulk rock chemistry and marking structures: (i) the metric-scale basic granulite and brown amphibolite lenses preserve the oldest recognised structures (i.e., S_1) while (ii) black amphibolites interlayered with metapelites mark the regional foliation (S_2).

Three deformation phases (D_1, D_2 and D_3) related to the H*T* evolution of the VP have been recognised. The oldest structures and stable assemblages (D_1 stage) preserved in basic granulite and

https://doi.org/10.1017/S0016756824000037 Published online by Cambridge University Press

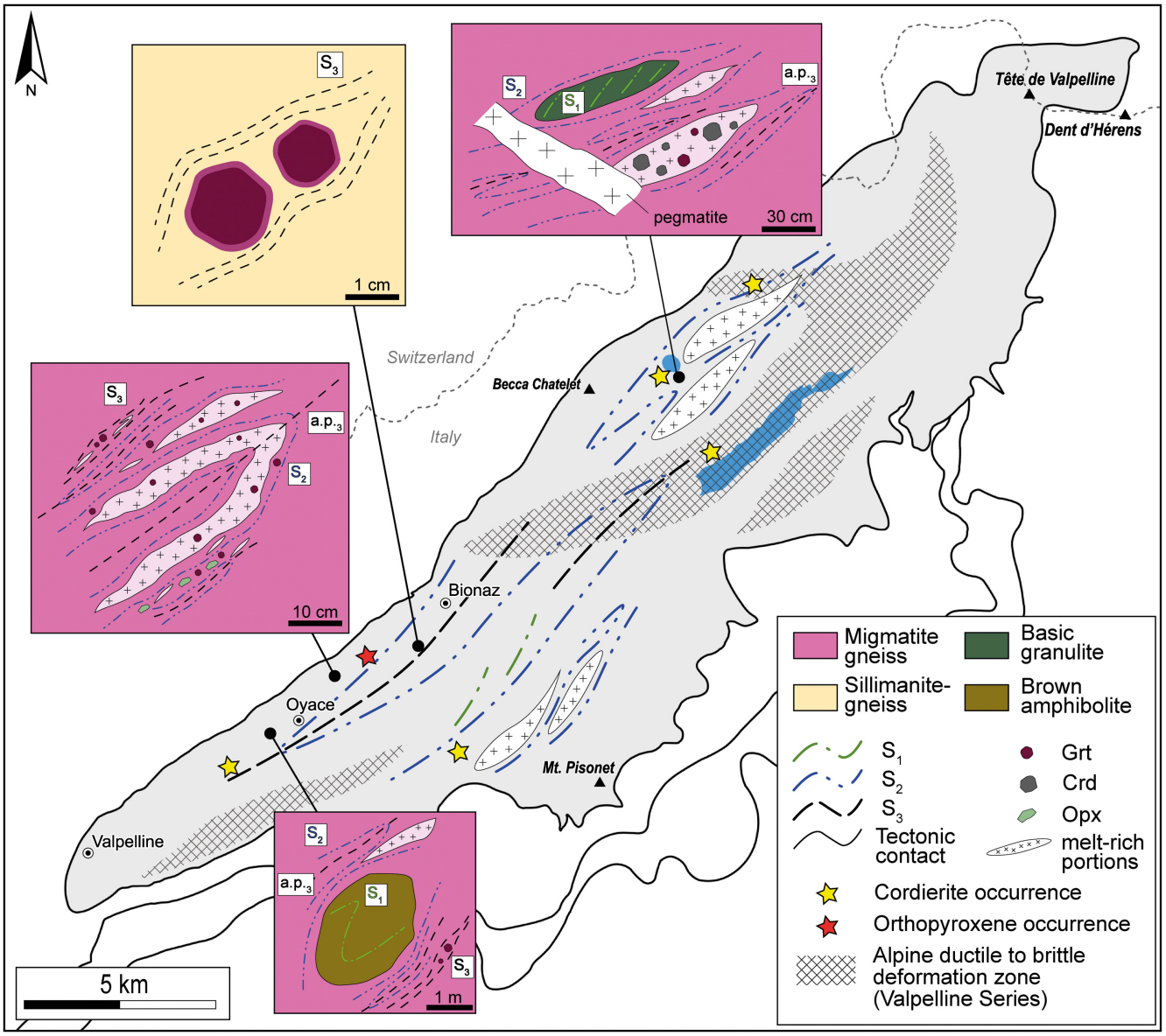

Figure 13. (Colour online) Simplified foliation traces map and sketches of key outcrops of the VP.

brown amphibolite boudins as an S_1 foliation (green foliation traces in Fig. 13) are locally discordant to the S_2 foliation pervasive in metapelites (green traces in Fig. 13). The evidence of D_1 is detected just in a few localities in the valley: (i) in brown amphibolite metre-scale lenses at Oyace; (ii) in basic granulites and brown amphibolites decametric to metric-scale lenses and boudins in Thoules (as previously also described by Manzotti & Zucali, 2013 as $S_{pre\text{-}2}$) and (iii) at Lac Mort area within basic granulites and brown amphibolites lenses or folded levels. The S_1, marked by the stable association of Amp I + Opx I + Cpx I + Pl I, is not accompanied by an extensive production of melt, except for rare microscale Pl + Grt-rich domains, which may indicate localised melting.

The D_2 tectono-metamorphic stage is related to the development of the S_2 regional foliation pervasive at the map-scale in metapelites, black amphibolites and metacarbonatic rocks (blue traces in Fig. 13). The S_2 is marked in migmatite gneiss by Bt+Sil+Grt (i.e., melanosomes) and quartz-feldspathic domains. These domains, interpreted as leucosomes, are parallel to the S_2 regional foliation at the micro-, meso- and map-scales and testify to widespread melt production at different scales during the D_2 stage. Leucosomes, which mark the D_2-related fabrics, contain garnet, cordierite and orthopyroxene (Fig. 13). These three phases are interpreted as peritectic products related to melt production. Garnet occurs widely in the VP rocks, while cordierite and orthopyroxene are detected only in some localities (see yellow and red stars in Fig. 13). In detail, cordierite occurs with garnet; orthopyroxene is also together with garnet, but an Opx–Crd-bearing assemblage has not been detected.

The S_2 foliation is reactivated during the D_3 stage, leading to its local transposition and development of the S_3 axial plane foliation (Fig. 13). The S_3 is pervasive in sillimanite-gneiss and in correspondence of m-wide localised high-strain domains in the migmatite gneiss; it wraps garnet, cordierite and orthopyroxene. Gardien *et al.* (1994) pointed out the presence of cordierite growing after regional foliation development. Conversely, our observations highlight that cordierite develops during the D_2 stage

https://doi.org/10.1017/S0016756824000037 Published online by Cambridge University Press

and is wrapped by the S_3 sillimanite-rich foliation (Caso, 2023). Due to the local isoclinal geometry of the D_3 folds, the S_3 (black lines in Fig. 13) and S_2 are parallel, striking NE–SW.

9.b. Litho-structural relationships with melt distribution in the lower crust

Analysing the geometrical relationships between different fabric elements distributed in diverse rock types is fundamental for understanding the generation and mobilisation of melt throughout the crust. Taking the VP as an example, each rock type in the lower crust exhibits diagnostic features and structures revealing information about different stages of the continental crust evolution and partial melting processes (i.e., melt production, subsequent differentiation in melt-rich and restitic portions, melt extraction and melt consumption; Kreigsman & Hensen, 1998; Waters, 2001; White & Powell, 2002; Kreigsman & Alvarez-Valero, 2010; Dyck *et al.* 2020; Yakymchuk, 2020).

As mentioned above, basic granulite (Fig. 14a) and brown amphibolite boudins (Fig. 14b and c), enclosed within metapelites and preserving the earlier mineral assemblages and structures, show little evidence of melt production. It is possible that the small amount of melt, eventually produced during the D_1 or D_2 stages, has been completely extracted thanks to the synchronous deformation, leaving a highly restitic rock made by amphibole, clino- and orthopyroxene and minor plagioclase.

The majority of metapelites in the studied area correspond to migmatite gneiss, characterised by a relatively high modal abundance of leucosomes (> 30%). Here, the boundary between leucosomes and fine-grained restitic lenses is frequently marked by biotite and sillimanite-rich selvedges, which may suggest limited melt extraction from these rocks and significant retrogression (Sawyer, 2008). The rounded quartz and biotite inclusions within garnet (i.e., Bt I and Qz I; Fig. 14d) provide evidence for its growth during melt production. This is possible according to the reaction Bt + Sil + Qz = Grt + Kfs + melt (Fig. 14d; Kriegsman & Alvarez-Valero, 2010; White *et al.* 2014). Relict and deformed Bt I and fibrous Sil I near or included in garnet porphyroblasts and separated by melt films (Fig. 14e) highlight the remnants of the biotite-dehydration melting reaction (Le Breton & Thompson, 1988). The same interpretation can be attributed to the few relict biotite and sillimanite grains re-oriented parallel to the S_2. The extensive partial melting during D_2 is also supported by the presence of myrmekites between quartz and plagioclase (Fig. 14f), diagnostic of melt production (e.g., Kreigsman & Alvarez-Valero, 2010). Felsic granulites made by garnet-rich domains, which mark the S_2 foliation, contain biotite or sillimanite in very low modal abundance. The few remnants of melt-related microstructures are recognisable only at the microscale as peritectic inclusions-rich garnet and plagioclase, and thin melt films along grain boundaries. They likely preserve the granulite-facies peak assemblage (i.e., Pl + Grt ± Rt), which may be due to significant melt-loss that prevented pervasive retrogression to lower temperature assemblages (e.g., White & Powell 2002). According to this hypothesis, felsic granulite could represent melt extraction during the D_2 (Voshage *et al.* 1990; Harlov & Wirth, 2000; White & Powell 2002). On the other hand, it also could be possible these rocks derived from a granitic mica-poor protolith which may not have produced a considerable (< 10%) amount of melt (Kreigsman & Alvarez-Valero, 2010; Sawyer, 2010).

Folded leucosomes within syn-D_3 fold hinges testify migration, during D_3, of the syn-D_2 melt towards the thickened hinges of these folds. Moreover, leucosomes are also localised within neck boudins. The transposition of the S_2 foliation is mainly localised in the sillimanite-gneiss, which is characterised by a pervasive continuous foliation (i.e., the S_3) marked by plurimillimetric prismatic sillimanite and minor biotite (Sil III and Bt III). This strong enrichment in sillimanite (Fig. 14g and h) that forms the pervasive foliation in sillimanite-gneiss could be produced in two ways: (i) destabilisation of white mica according to the reaction Ms + Qz = Sil + Kfs + melt or (ii) during retrogression in the presence of melt by back-crossing the reaction Bt + Sil + Qz + Pl = Grt + Crd + Kfs + melt (Waters, 1988; Waters, 2001; Kreigsman & Alvarez-Valero, 2010; White *et al.* 2014). The S_3 sillimanite-rich foliation wraps peritectic mineral as garnet (Manzotti & Zucali, 2013) and cordierite (Caso, 2023), likely represents the back-reaction with melt (Spear, 1994; Kriegsman & Alvarez-Valero, 2010) involving garnet and cordierite. The intergrowths between quartz and biotite marking S_3 and wrapping cordierite or orthopyroxene (Fig. 14i) are also commonly interpreted as back-reaction products (Sawyer, 1999; Waters, 2001; Kreigsman & Alvarez-Valero, 2010). Therefore, S_3 may represent a preferential pathway for both melt migration and its interaction with the peritectic minerals.

The quartz-feldspathic layers or lenses, found in black amphibolite, contain clinopyroxene and/or garnet porphyroblasts, which could represent peritectic minerals as the product of partial melting through fluid-absent incongruent hornblende breakdown. Melt production in metabasic rocks needs sufficiently high temperatures to take place (> 800 °C; Rushmer, 1991; Wyllie & Wolf, 1993; Kunz *et al.* 2014) similar to those obtained through the Ti-in-amphibole thermometry. Since leucosomes of black amphibolite are parallel to S_2 foliation, it can be inferred that melting has occurred during the D_2 stage in amphibolites as well.

9.c. Thermal state during melt-production and migmatisation

Temperatures derived from different geothermometers differ depending on the methods used and vary across different localities. However, systematic variations exist among the different lithologies. Particularly evident is the temperature difference of ~100 °C between metapelites (peak temperature ca. 760 °C) and amphibolites (peak temperature ca. 860 °C, locally up to 900 °C; Figs. 11 and 12). This marked difference may occur since biotite was no longer stable at the maximum reached temperature and therefore was not able to register peak temperatures like amphibole did. In fact, the biotite-dehydration melting (here testified by relicts Bt I) occurs at lower temperatures (Le Breton & Thompson, 1988) than amphibole-dehydration melting. Temperatures derived from biotite marking the S_3 foliation growing together with sillimanite after garnet, cordierite or orthopyroxene that reacted with melt during cooling after peak (Bt III; Stüwe, 1997; Kreigsman & Hensen, 1998; Brown, 2002; Kreigsman & Alvarez Valero, 2010), are equal to those from Bt I and Bt II. Most of the temperatures derived from the garnet–biotite Fe–Mg exchange thermometer (Ferry & Spear, 1978) provide lower values (with a minimum of ~560 °C). These values are related to late diffusional resetting after peak metamorphic conditions, and thus after D_2/D_3 stages (Pattison *et al.* 2003 and references therein).

A temperature variation is visible among the different migmatite gneisses (i.e., Grt-, Crd- and Opx-bearing), with the highest temperatures calculated for Opx-bearing gneiss (up to ~810 °C) and the lowest ones in Crd-bearing migmatites (750 °C; Fig. 15). However, these differences are relatively small, with values

https://doi.org/10.1017/S0016756824000037 Published online by Cambridge University Press

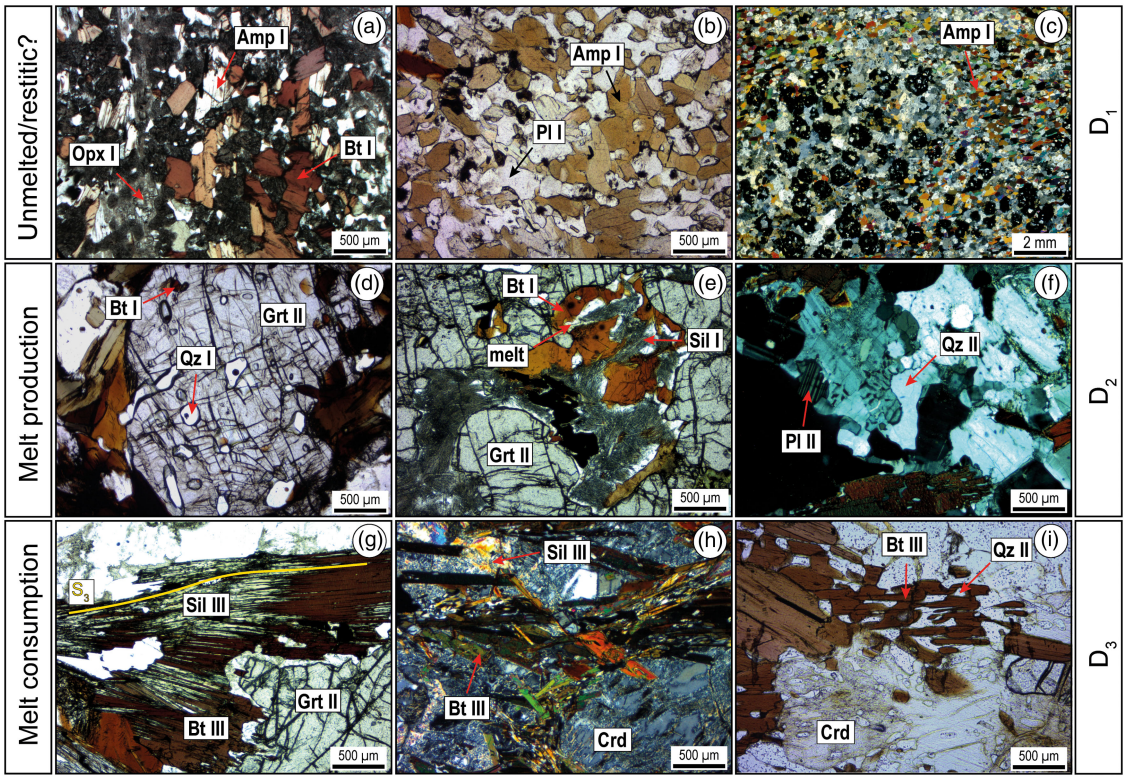

Figure 14. (Colour online) Diagnostic microstructrures related to the migmatisation: (a) Opx I, Bt I and Amp I in basic granulite boudin (XPL). (b) Amp I and Pl I in brown amphibolite (PPL). (c) Grt + Pl-rich domain in brown amphibolite (XPL). (d) Grt II porphyroblast rich in rounded Qz I inclusions (PPL). (e) Relict deformed Bt I and fibrous Sil I reacting to produce melt and Grt II (PPL). (f) Myrmekites between Pl and Qz (XPL). (g) Sil III and Bt III S_3 foliation growing after Grt porphyroblast (PPL). (h) Bt III and Sil III growing over Crd (XPL). (i) Bt III and Qz II intergrowth after Crd (PPL).

close to the error of each method, i.e., ±50 °C at > 700 °C (see Table 2 standard deviation and Henry *et al.* 2005).

Partial Alpine retrogressions could also explain temperature variations in metapelites, where such retrogressions are localised along hectometre-wide Alpine-age deformation horizons (Fig. 2) of widespread greenschist-facies overprinting (Manzotti *et al.* 2014; Dal Piaz *et al.* 2016). These deformation zones could separate different domains within the VP that underwent different *P–T* conditions, explaining the temperature variation between Crd- and Oxp-bearing migmatites. According to the present map of rock distribution and Alpine horizons (Figs. 2 and 13), the reviewed temperature differences do not seem to be controlled by the Alpine horizons. Indeed, similar differences are recorded at the Lac Mort area, north of one km-scale Alpine horizons and at the Oyace area (Fig. 13).

9.d. Tectono-metamorphic evolution of the Valpelline series

The VP preserves a complex polyphasic evolution spanning from the pre-Alpine to Alpine age, under amphibolite-/granulite- to greenschist-facies conditions. The oldest remnants of the earlier tectono-metamorphic stage (D_1) have been detected in the basic granulite and amphibolite boudins within metapelites. An earlier subsolidus stage before partial melting occurring during the D_1 or early D_2 is preserved in garnet cores as relict biotite, sillimanite, plagioclase and rutile, included in porphyroblasts. Manzotti & Zucali (2013) provided thermobarometric estimates of this event at $T = 700 \pm 50$ °C and $P = 0.57 \pm 0.1$ GPa (MZ1 in Fig. 15). Different values have been obtained by Gardien *et al.* (1994), who fixed the *P–T* condition of their oldest stage at higher pressure (G1 in Fig. 15) from kyanite relicts within garnet cores ($P = 0.9$–0.1 GPa).

The D_2 stage during which partial melting occurs, is accompanied by garnet, cordierite or orthopyroxene growth in metapelites yielding different temperatures (considering the Ti-in-biotite thermometer). The temperature range of 650–780 °C obtained from cordierite-migmatites intersects the biotite-dehydration melting reaction (Le Breton & Thompson, 1988; Spear, 1994; Waters, 2001; White *et al.* 2014). Pressures obtained using the Grt–Crd barometer (Bhattacharya, 1986) of 0.58 ± 0.01 GPa and fall within the *P* range defined by the peak assemblage of a similar cordierite-metapelite from the IVZ (Redler *et al.* 2012) using thermodynamic modelling (orange field in Fig. 15). Temperatures obtained from orthopyroxene-bearing migmatites using the Ti-in-biotite thermometer, ranging between 700 and 830 °C, also fit with the peak assemblage and *P–T* conditions detected in similar samples in the IVZ by Redler *et al.* (2012) (blue field in Fig. 15) but at higher pressure ($P = 0.8$ GPa) respect to the cordierite-bearing ones. Temperatures yielded by black amphibolite using the Ti-in-Amp thermometer of Liao *et al.* (2021) range between 800 and 930 °C. These values, ~100 °C higher than metapelites agree with the destabilisation of hornblende at $\sim T > 900$ °C (dashed black line in Fig. 15), meaning that amphibolite recorded higher temperature conditions. Pressures obtained from black amphibolite for the D_2 stage applying the Amp–Pl geobarometer (Molina *et al.* 2015) range between ~0.7 and 1.2 GPa (Fig. 15).

https://doi.org/10.1017/S0016756824000037 Published online by Cambridge University Press

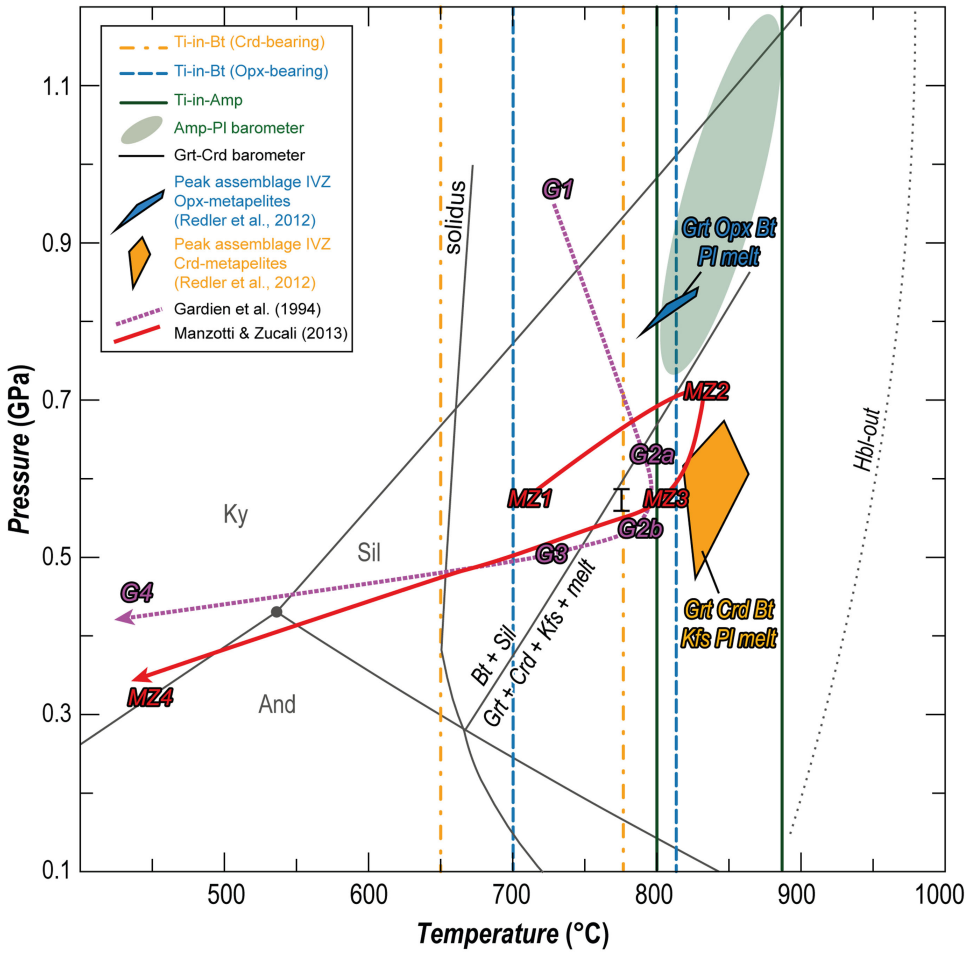

Figure 15. (Colour online) *P–T* conditions of VP. Pl–Amp barometer calibration of Molina *et al.* (2015); Grt–Crd barometer of Bhattacharya (1986).

The thermal conditions during the D_2 and D_3 stages in metapelites are similar since the Ti-in-Bt thermometry applied on biotite marking both S_2 and S_3 foliations yielded similar *T* °C values. In fact, these values should be considered only as minimum temperatures (up to 800 °C) related to the D_2 and D_3 phases, i.e., slightly before biotite destabilisation due to incongruent melting (D_2) or related to melt consumption and back reaction with peritectic minerals (D_3) producing biotite. The *T* °C range of black amphibolites coincides with one of the D_2 and D_3 stages of Manzotti & Zucali (2013; MZ2 and MZ3 in Fig. 15) and the *P–T* peak conditions of similar cordierite- and orthopyroxene-bearing metapelites from the IVZ from Redler *et al.* (2012). Taking this into account is possible to constrain the *P–T* conditions for melt production and consumption. The *T* °C range is comprised between ~800 and 900 °C and the *P* between ~0.5 and 0.8 GPa. The field of orthopyroxene-bearing migmatites from the Val Strona (IVZ), determined by Redler *et al.* (2012, 2013), can be used as upper pressure limit.

The inferred metamorphic conditions and *P–T* paths for the VP lower continental crust are compatible with an evolution typical to many high-grade terranes related to extensional geodynamic settings: prograde to peak metamorphic conditions reaching and overstepping the suprasolidus conditions, followed by nearly isobaric heating (Jiao *et al.* 2023 and references therein). This could explain the close *P–T* conditions and similar mineral assemblage stability during the D_2 and D_3 events. However, the detection of kyanite in garnets by Gardien *et al.* (1994) shifting the early path to higher pressure conditions followed by decompression heating may highlight a more complex evolution probably linked to Variscan orogenic crustal thickening during the Carboniferous (Carosi *et al.* 2020; Schulmann *et al.* 2022; Roda *et al.* 2023) and subsequent orogenic collapse and lithospheric extension during late Carboniferous-Permian (Lardeaux & Spalla, 1991; Marotta & Spalla, 2007; Schuster & Stuwe, 2008; Roda *et al.* 2018; Ewing *et al.* 2023).

9.e Geodynamic implications for the Adria lower continental crust: comparison with the Ivrea-Verbano Zone lower crustal section

The IVZ (Southern Alpine Domain) and the IIDK (Austroalpine Domain), both belonging to the Adria microplate, have several similarities with the VP in terms of rock types, *P–T* conditions, and ages of metamorphism.

Metapelites, felsic granulite (usually named 'stronalites'; Redler *et al.* 2012) and black amphibolite with localised partial melting (Kunz *et al.* 2014) occur both in the VP and IVZ. The bulk rock compositions of both VP and IVZ metapelites and metabasite are also similar (Fig. 8). However, an important difference with the IVZ lies in the distribution of the three migmatite types (i.e., Grt-, Crd- and Opx-bearing) and in the map-scale continuity of the isograds, with higher-grade

https://doi.org/10.1017/S0016756824000037 Published online by Cambridge University Press

conditions approaching the Insubric Line (i.e., from the Ms- to Opx isograds). In fact, the VP rock types crop out without a clear crustal zonation unlike the IVZ, where the different parageneses reflect a clear metamorphic zonation. Moreover, prograde muscovite occurring in IVZ migmatites is lacking in the VP ones. The only remnant of prograde dehydration melting reactions is the relict biotite included within peritectic phases or deformed biotite grains scattered within the rock matrix.

The thermal state described in the IVZ with similar methods used in the present work (i.e., the Zr-in-Rt; Ewing *et al.* 2013) is comparable with the one described in the VP. However, in the IVZ, higher temperatures reaching 1000 °C have been locally detected close to the contact with the Mafic Complex (Barbooza & Bergantz, 2000; Luvizotto & Zack, 2009). Conversely, the VP never reached the same UH*T* conditions, suggesting that no mafic bodies were in place close by and large enough to produce such temperatures in the VP rocks. For this reason, the VP represents a good case study to investigate the regional Permian metamorphism without the effects of contact metamorphism.

The few available ages for the VP metapelites obtained through U-Pb geochronology on zircon and monazite yielded late Carboniferous and Permian ages (Zucali *et al.* 2011; Pesenti *et al.* 2012; Kunz *et al.* 2018), similar to those for the IVZ (Barbooza *et al.* 1999; Peressini *et al.* 2007; Ewing *et al.*, 2013; Williams *et al.*, 2022). In particular, Kunz *et al.* (2018) provided two groups of ages by dating zircons from VP migmatites of ~290–280 Ma and ~270 Ma. Permian ages are also found in the Arolla Series granitoids and orthogneiss (~290 Ma; Bussy *et al.* 1998; Manzotti *et al.* 2018). This geochronological link between the VP H*T* metamorphism and magmatism in the neighbouring Arolla Series could explain partial melting occurring in the VP lower crust and the emplacement of granitic intrusions in the Arolla Series upper crust (Kunz *et al.* 2018).

10. Conclusions

This work provides a detailed lithological and structural overview of the VP, with a focus on its Permian tectono-metamorphic evolution. The obtained results are summarised as follows:

- The VP represents a lower continental crust sector, belonging to the Dent-Blanche Nappe in the Western Alps that preserves pre-Alpine structures and mineral assemblages.
- The pervasive distribution of migmatite-bearing structures in the VP rocks testifies that this unit was part of a km-scale migmatitic terrane involved in high-grade metamorphism during Permian lithospheric extension and asthenosphere rising, linked with abundant melt production, which migrated from its source to shallower crustal levels.
- Migmatite gneiss shows three different mineral assemblages i.e., (i) Grt-bearing; (ii) Crd–Grt-bearing and (iii) Opx–Grt-bearing associated with slightly different *P*–*T* conditions.
- The VP shows rock types, *P*–*T* conditions and ages of partial melting similar to IVZ, but lacks the presence of potential heat sources like the Mafic Complex occurring in the IVZ associated with locally higher peak-*T*.
- *P*–*T* conditions of the migmatisation in the VP are between 800–900 °C and 0.5–0.8 GPa.

Supplementary material

To view supplementary material for this article, please visit https://doi.org/10.1017/S0016756824000037

Acknowledgements. We would like to thank Prof. Federico Farina and Dr. Marco Filippi for their suggestions on the first draft of the manuscript. Dr. Francesco Nosenzo and an anonymous reviewer are also thanked for their constructive reviews and suggestions. Many thanks also to Dr. Simon Schorn for his editorial work and useful suggestions. The results here presented have been developed in the frame of the MIUR Project 'Dipartimenti di Eccellenza 2017—Le Geoscienze per la società: risorse e loro evoluzione (work package 3, tasks 3.3 and 3.4)'. The work was partly supported by the Italian Ministry for Universities and Research through the project 'Dipartimenti di Eccellenza 2023-27'.

Financial support. This research has been funded by 'PSR2020_MRODA'.

Competing interests. The authors declare no conflict of interest.

References

Angrand P and Mouthereau F (2021) Evolution of the Alpine orogenic belts in the Western Mediterranean region as resolved by the kinematics of the Europe-Africa diffuse plate boundary. *BSGF-Earth Sciences Bulletin* **192**, 42. doi: 10.1051/bsgf/2021031

Argand E (1906) Sur la tectonique du Massif de la Dent Blanche. *Comptes Rendus de l'Académie des Sciences Paris* **142**, 527–30.

Barboza SA and Bergantz GW (2000) Metamorphism and anatexis in the mafic complex contact aureole, Ivrea Zone, Northern Italy. *Journal of Geology* **41**, 1307–27. doi: 10.1093/petrology/41.8.1307

Barboza SA, Bergantz GW and Brown M (1999) Regional granulite facies metamorphism in the Ivrea zone: is the Mafic Complex the smoking gun or a red herring? *Geology* **27**, 447–50. doi: 10.1130/0091-7613(1999)027%3C0447:RGFMIT%3E2.3.CO;2

Beltrando M, Compagnoni R and Lombardo B (2010) (Ultra-) High-pressure metamorphism and orogenesis: an Alpine perspective. *Gondwana Research* **18**, 147–66. doi: 10.1016/j.gr.2010.01.009

Bhattacharya A (1986) Some geobarometers involving cordierite in the FeO–Al_2O_3–SiO_2(+H_2O) system: refinements, thermodynamic calibration, and applicability in granulite facies rocks. *Contributions to Mineralogy and Petrology* **94**, 387–94. doi: 10.1007/BF00371446

Bohlen SR (1987) Pressure-temperature-time paths and a tectonic model for the evolution of granulites. *Journal of Geology* **95**, 617–32. doi: 10.1086/629159

Bousquet R, Oberhänsli R, Goffé B, Wiederkehr M, Koller F, Schmid SM, Schuster R, Engi M, Berger A and Martinotti G (2008) Metamorphism of metasediments at the scale of an orogen: a key to the Tertiary geodynamic evolution of the Alps. *Geological Society, London, Special Publications* **298**, 393–411.

Brown M (2002) Prograde and retrograde processes in migmatites revisited. *Journal of Metamorphic Geology* **20**, 25–40. doi: 10.1046/j.0263-4929.2001.00362.x

Bussy F, Venturini G, Hunziker J and Martinotti G (1998) U-Pb ages of magmatic rocks of the western Austroalpine Dent- Blanche-Sesia Unit. *Schweizerische Mineralogische Und Petrographische Mitteilungen* **78**, 16. doi: 10.1144/SP298.18

Carosi R, Petroccia A, Iaccarino S, Simonetti M, Langone A and Montomoli C (2020) Kinematics and timing constraints in a transpressive tectonic regime: the example of the Posada-Asinara Shear Zone (NE Sardinia, Italy). *Geosciences* **10**, 288. doi: 10.3390/geosciences10080288

Carraro F, Dal Piaz GV and Sacchi R (1970) Serie di Valpelline e II Zona Diorito-Kinzigitica sono i relitti di un ricoprimento proveniente dalla Zona Ivrea-Verbano. *Memorie della Società Geologica Italiana* **9**, 197–224.

Caso F (2023) Quantitative combined multiscale structural and minero-chemical analysis to unravel the tectono-metamorphic evolution of cordierite-migmatite gneiss from the Valpelline Unit (Dent-Blanche Nappe, Western Italian Alps, Valle d'Aosta). *Rendiconti Online della Società Geologica Italiana* **60**. doi: 10.3301/ROL.2023.20

Caso F, Nerone S, Petroccia A and Bonasera M (2021) Geology of the southern Gran Paradiso Massif and Lower Piedmont Zone contact area (middle Ala Valley, Western Alps, Italy). *Journal of Maps* **17**, 237–46. doi: 10.1080/17445647.2021.1911869

Dal Piaz GV (1999) The Austroalpine-Piedmont nappe stack and the puzzle of Alpine Tethys. *Memorie di Scienze Geologiche* **51**, 155–76.

Dal Piaz GV, Bistacchi A, Gianotti F, Monopoi B, Passeri L and Schivo A (2016) Note illustrative del F. 070 Monte Cervino della Carta geologica d'Italia alla scala 1:50.000. *Memorie Descrittive Carta Geologica D'Italia* **101**, 5–258.

Deer WA, Howie RA and Zussman J (1996) *An Introduction to the Rock-Forming Minerals*. New York: John Wiley and Sons, 1–528.

Diehl EA, Masson R and Stutz AH (1952) Contributo alla conoscenza del ricoprimento della Dent Blanche. *Memorie degli Istituti di Geologia e Mineralogia dell'Università di Padova* **17**, 1–52.

Dyck B, Waters DJ, St-Onge WR and Searle MP (2020) Muscovite dehydration melting: reaction mechanisms, microstructures, and implications for anatexis. *Journal of Metamorphic Geology* **38**, 29–52. doi: 10.1111/jmg.12511

Ewing TA, Hermann J and Rubatto D (2013) The robustness of the Zr-inrutile and Ti-in-zircon thermometers during high-temperature metamorphism (Ivrea-Verbano Zone, northern Italy). *Contribution to Mineralogy and Petrology* **165**, 757–79. doi: 10.1007/s00410-012-0834-5

Ewing TA, Rubatto D, Beltrando M and Hermann J (2015) Constraints on the thermal evolution of the Adriatic margin during Jurassic continental break-up: U-Pb dating of rutile from the Ivrea-Verbano Zone, Italy. *Contribution to Mineralogy and Petrology* **169**, 1–22. doi: 10.1007/s00410-015-1135-6

Ewing TA, Rubatto D, Lemke K and Hermann J (2023) Timescales and mechanisms of felsic lower continental crust formation: Insights from U-Pb geochronology of detrital zircon (Malenco Unit, eastern Central Alps). *Lithos* **456–457**, 107286. doi: 10.1016/j.lithos.2023.107286

Ferry JM and Spear FS (1978) Experimental calibration of the partitioning of Fe and Mg between biotite and garnet. *Contributions to Mineralogy and Petrology* **66**, 113–7. doi: 10.1007/bf00372150

Gardien V, Reusser E and Marquer D (1994) Pre-Alpine metamorphic evolution of the gneisses from the Valpelline Series (Western Alps, Italy). *Schweizerische Mineralogische und Petrographische Mitteilungen* **74**, 489–502.

Giuntoli F and Engi M (2016) Internal geometry of the central Sesia Zone (Aosta Valley, Italy): HP tectonic assembly of continental slices. *Swiss Journal of Geosciences* **109**, 445–71. doi: 10.1007/s00015-016-0225-4

Hacker BR, Kelemen PB and Behn MD (2015) Continental lower crust. *Annual Review of Earth and Planetary Sciences* **43**, 167–205. doi: 10.1146/annurev-earth-050212-124117

Handy MR, Schmid SM, Bousquet R, Kissling E and Bernoulli D (2010) Reconciling plate-tectonic reconstructions of Alpine Tethys with the geological-geophysical record of spreading and subduction in the Alps. *Earth-Science Reviews* **102**, 121–58. doi: 10.1016/j.earscirev.2010.06.002

Harlov D and Wirth R (2000) K-feldspar–quartz and K-feldspar–plagioclase phase boundary interactions in garnet–orthopyroxene gneiss's from the Val Strona di Omegna, Ivrea–Verbano Zone, northern Italy. *Contribution to Mineralogy and Petrology* **140**, 148–62. doi: 10.1007/s004100000185

Hawkesworth CJ, Cawood PA and Dhuime B (2020) The evolution of the continental crust and the onset of plate tectonics. *Frontiers in Earth Sciences* **8**, 326. doi: 10.3389/feart.2020.00326

Hawthorne FC, Oberti R, Harlow GE, Maresch WV, Martin RF, Schumacher JC and Welch MD (2012) Nomenclature of the amphibole supergroup. *American Mineralogist* **97**, 2031–48. doi: 10.2138/am.2012.4276

Henry B, Guidotti CV and Thomson JA (2005) The Ti-saturation surface for low-to-medium pressure metapelitic biotite: implications for geothermometry and Ti-substitution mechanisms. *American Mineralogist* **90**, 316–28. doi: 10.2138/am.2005.1498

Jiao S, Brown M, Mitchell RN, Chowdhury P, Clark C, Chen L, Chen Y, Korhonene F, Huang G and Guo J (2023) Mechanisms to generate ultrahigh-temperature metamorphism. *Nature Reviews Earth & Environment* **4**, 298–318. doi: 10.1038/s43017-023-00403-2

Johnson SE and Vernon RH (1995) Inferring the timing of porphyroblast growth in the absence of continuity between inclusion trails and matrix foliations: can it be reliably done? *Journal of Structural Geology* **17**(8), 1203–6. doi: 10.1016/0191-8141(95)00021-5

Kreigsman LM and Hensen BJ (1998) Back reaction between restite and melt: Implications for geothermobarometry and pressure-temperature paths. *Geology* **26**, 1111–4. doi: 10.1130/0091-7613(1998)026%3C1111:BRBRAM%3E2.3.CO;2

Kriegsman LM and Alvarez-Valero AM (2010) Meltproducing versus melt-consuming reactions in pelitic xenoliths and migmatites. *Lithos* **116**, 310–20. doi: 10.1016/j.lithos.2009.09.001

Kunz BE, Johnson TE, White RW and Redler C (2014) Partial melting of metabasic rocks in Val Strona di Omegna, Ivrea Zone, northern Italy. *Lithos* **190-191**, 1–12. doi: 10.1016/j.lithos.2013.11.015

Kunz BE, Manzotti P, von Niederhäusern B, Engi M, Darling JR, Giuntoli F and Lanari P (2018) Permian high-temperature metamorphism in the Western Alps (NW Italy). *International Journal of Earth Sciences* **107**, 203–29. doi: 10.1007/s00531-017-1485-6

Lardeaux JM and Spalla MI (1991) From granulites to eclogites in the Sesia Zone (Italian Western Alps) – a record of the opening and closure of the Piedmont Ocean. *Journal of Metamorphic Geology* **9**, 35–59. doi: 10.1111/j.1525-1314.1991.tb00503.x

Law RD (2014) Deformation thermometry based on quartz c-axis fabrics and recrystallization microstructures: a review. *Journal of structural Geology* **66**, 129–61. doi: 10.1016/j.jsg.2014.05.023

Le Breton NL and Thompson AB (1988) Fluid-absent (dehydration) melting of biotite in metapelites in the early stages of crustal anatexis. *Contribution to Mineralogy and Petrology* **99**, 226–37. doi: 10.1007/BF00371463

Liao Y, Wei C and Rehman HU (2021) Titanium in calcium amphibole: behavior and thermometry. *American Mineralogist* **106**, 180–91. doi: 10.2138/am-2020-7409

Luoni P, Rebay G, Roda M, Zanoni D and Spalla MI (2020) Tectono-metamorphic evolution of UHP Zermatt-Saas serpentinites: a tool for vertical palaeogeographic restoration. *International Geology Review* **63**, 1236–61. doi: 10.1080/00206814.2020.1758967

Luvizotto GL and Zack T (2009) Nb and Zr behavior in rutile during high-grade metamorphism and retrogression: an example from the Ivrea-Verbano Zone. *Chemical Geology* **261**, 303–17. doi: 10.1016/j.chemgeo.2008.07.023

Manzotti P and Ballèvre M (2017) Tectonic history of the Dent Blanche. *Geological Field Trips and Maps* **9**, 73. doi: 10.3301/GFT.2017.02

Manzotti P, Ballèvre M, Pitra P, Benita Putlitz P, Robyr M and Müntener O (2020) The growth of sodic amphibole at the Greenschist- to Blueschist-facies transition (Dent Blanche, Western Alps): Bulk-rock chemical control and thermodynamic modelling." *Journal of Petrology* **61**. doi: 10.1093/petrology/egaa044

Manzotti P, Ballèvre M, Zucali M, Robyr M and Engi M (2014) The tectonometamorphic evolution of the Sesia–Dent Blanche nappes (internal Western Alps): review and synthesis. *Swiss Journal of Geosciences* **107**, 309–36. doi: 10.1007/s00015-014-0172-x

Manzotti P, Rubatto D, Zucali M, El Kohr A, Cenki-Tok B, Ballèvre M and Engi M (2018) Permian magmatism and metamorphism in the Dent Blanche nappe: constraints from field observations and geochronology. *Swiss Journal of Geosciences* **111**, 79–97. doi: 10.1007/s00015-017-0284-1

Manzotti P and Zucali M (2013) The pre-Alpine tectonic history of the Austroalpine continental basement in the Valpelline unit (Western Italian Alps). *Geological Magazine* **150**, 153–72. doi: 10.1017/S0016756812000441

Marotta AM and Spalla MI (2007) Permian-Triassic high thermal regime in the Alps: result of late Variscan collapse or continental rifting? Validation by numerical modeling. *Tectonics* **26**, TC4016. doi: 10.1029/2006TC002047

Molina JF, Moreno JA, Castro A, Rodríguez C and Fershtater GB (2015) Calcic amphibole thermobarometry in metamorphic and igneous rocks: new calibrations based on plagioclase/amphibole Al-Si partitioning and amphibole/liquid Mg partitioning. *Lithos* **232**, 286–305. doi: 10.1016/j.lithos.2015.06.027

Morimoto N, Fabries J, Ferguson AK, Ginzburg I, Ross VM, Seifert FA, Zussman J, Aoki K and Gottardi G (1988) Nomenclature of pyroxenes. *American Mineralogist* **73**, 1123–33.

Nicot E (1977) Les roches meso et catazonales de la Valpelline (nappe de la Dent Blanche, Alpes italiennes) (PhD Thesis, Paris).

Passchier CW and Trouw RAJ (2005) *Microtectonics*. Berlin, Heidelberg: Springer, p. 366. doi: 10.1007/3-540-29359-0

Pattison DR, Chacko T, Farquhar J and Mcfarlane CR (2003) Temperatures of granulite-facies metamorphism: constraints from experimental phase

equilibria and thermobarometry corrected for retrograde exchange. *Journal of Petrology* **44**, 867–900. doi: 10.1093/petrology/44.5.867

Pennacchioni G and Guermani A (1993) The mylonites of the Austroalpine Dent Blanche nappe along the northwestern side of the Valpelline Valley (Italian Western Alps). *Memorie di Scienze Geologiche* **45**, 37–55.

Peressini G, Quick JE, Sinigoi S, Hofmann AW and Fanning M (2007) Duration of a large mafic intrusion and heat transfer in the lower crust: a SHRIMP U–Pb zircon study in the Ivrea–Verbano Zone (Western Alps, Italy). *Journal of Petrology* **48**, 1185–218. doi: 10.1093/petrology/egm014

Pesenti C, Zucali M, Manzotti P, Diella V and Risplendente A (2012) Linking U-Th-Pb monazite dating to partial melting microstructures: application to the Valpelline series (Austroalpine domain, Western Alps). *Rendiconti Online Società Geologica Italiana* **22**, 183–5.

Pognante U (1979) The Orsiera-Rocciavrè metaophiolitic complex (Italian Western Alps). *Ofioliti* **4**, 183–98.

Quick JE, Sinigoi S, Snoke AW, Kalakay TJ, Mayer A and Peressini G (2003) Geologic map of the southern Ivrea-Verbano Zone, Northwestern Italy. *USGS, Washington, DC* **I-2776**, 1–22.

Redler C, Johnson TE, White RW and Kunz BE (2012) Phase equilibrium constraints on a deep crustal metamorphic field gradient: metapelitic rocks from the Ivrea Zone (NW Italy). *Journal of Metamorphic Geology* **30**, 235–54. doi: 10.1111/j.1525-1314.2011.00965.x

Redler C, White RW and Johnson TE (2013) Migmatites in the Ivrea Zone (NW Italy): constraints on partial melting and melt loss in metasedimentary rocks from Val Strona di Omegna. *Lithos* **175–176**, 40–53. doi: 10.1016/j.lithos.2013.04.019

Roda M, Regorda A, Spalla MI and Marotta AM (2018) What drives Alpine Tethys opening? Clues from the review of geological data and model predictions. *Geological Journal* **54**, 2646–64. doi: 10.1002/gj.3316

Roda M, Spalla MI, Filippi M, Lardeaux J-M, Rebay G, Regorda A, Zanoni D, Zucali M and Gosso G (2023) Metamorphic remnants of the Variscan Orogeny across the alps and their tectonic significance. *Geosciences* **13**, 300. doi: 10.3390/geosciences13100300

Roda M and Zucali M (2008) Meso and microstructural evolution of the Mont Morion metaintrusives complex (Dent Blanche nappe, Austroalpine domain, Valpelline, Western Italian Alps). *Italian Journal of Geosciences* **127**, 105–23.

Roda M, Zucali M, Corti L, Visalli R, Ortolano G and Spalla MI (2021) Blueschist mylonitic zones accommodating syn-subduction exhumation of deeply buried continental crust: the example of the Rocca Canavese Thrust Sheets Unit (Sesia-Lanzo Zone, Italian Western Alps). *Swiss Journal of Geosciences* **114**, 6–39. doi: 10.1186/s00015-021-00385-7

Rushmer T (1991) Partial melting of two amphibolites: contrasting experimental results under fluid absent con-ditions. *Contributions to Mineralogy and Petrology* **107**, 41–59. doi: 10.1007/BF00311184

Sawyer EW (1999) Criteria for the recognition of partial melting. *Physics and Chemistry of the Earth Part A-Solid Earth and Geodesy (A)* **24**, 269–79. doi: 10.1016/S1464-1895(99)00029-0

Sawyer EW (2008) *Working with Migmatites*. Short Course Series: Mineralogical Association of Canada, volume 38. Quebec: Mineralogical Association of Canada, 158 pp.

Sawyer EW (2010) Migmatites formed by water-fluxed partial melting of a leucogranodiorite protolith: Microstructures in the residual rocks and source of the fluid. *Lithos* **116**, 273–86. doi: 10.1016/j.lithos.2009.07.003

Schmid SM, Aebli HR, Heller F and Zingg A (1989) The role of the periadriatic line in the tectonic evolution of the alps. In Alpine Tectonics (eds MP Coward, D Dietrich & RG Park), 45, pp. 153–171: Geological Society, London, Special Publications.

Schmid SM, Fügenschuh B, Kissling E and Schuster R (2004) Tectonic map and overall architecture of the Alpine orogen. *Eclogae Geologicae Helvetiae* **97**, 93–117. doi: 10.1007/s00015-004-1113-x

Schulmann K, Edel JB, Catalán JRM, Mazur S, Guy A, Lardeaux JM, Ayarza P and Palomeras I (2022) Tectonic evolution and global crustal architecture of the European Variscan belt constrained by geophysical data. *Earth-Science Reviews*, 104195. doi: 10.1016/j.earscirev.2022.104195

Schuster R and Stüwe K (2008) Permian metamorphic event in the alps. *Geology* **36**, 603–6. doi: 10.1130/G24703A.1

Spalla MI, Zucali M, Di Paola S and Gosso G (2005) A critical assessment of the tectono-thermal memory of rocks and definition of tectono-metamorphic units: evidence from fabric and degree of metamorphic transformations. *Geological Society, London, Special Publications* **243**, 227–47. doi: 10.1144/GSL.SP.2005.243.01.16

Spear F (1994) *Metamorphic Phase Equilibria and Pressure-Temperature-Time Paths*. Mineralogical Society Monographs, 799 pp.

Stipp M, Stünitz H, Heilbron M and Schmid DW (2002) The eastern tonale fault zone: a natural laboratory for crystal plastic deformation of quartz over a temperature range from 250 to 700 °C. *Journal of Structural Geology* **24**, 1861–84. doi: 10.1016/S0191-8141(02)00035-4

Stüwe K (1997) Effective bulk composition changes due to cooling: a model predicting complexities in retrograde reaction+textures. *Contributions to Mineralogy and Petrology* **129**, 43–52. doi: 10.1007/s004100050322

Tomkins HS, Powell R and Ellis DJ (2007). The pressure dependence of the zirconium-in-rutile thermometer. *Journal of Metamorphic Geology* **25**, 703–13. doi: 10.1111/j.1525-1314.2007.00724.x

Touret JLR, Santosh M and Huizenga JM (2022) Composition and evolution of the continental crust: Retrospect and prospect. *Geoscience Frontiers* **13**, 101428. doi: 10.1016/j.gsf.2022.101428

Voshage H, Hofmann A, Mazzucchelli M, Rivalenti G, Sinigoi S, Raczek I and Demarchi G (1990) Isotopic evidence from the Ivrea Zone for a hybrid lower crust formed by magmatic underplating. *Nature* **347**, 731–6. doi: 10.1038/347731a0

Waters DJ (1988) Partial melting and the formation of granulite facies assemblages in Namaqualand, South Africa. *Journal of Metamorphic Geology* **6**, 387–404. doi: 10.1111/j.1525-1314.1988.tb00430.x

Waters DJ (2001) The significance of prograde and retrograde quartz-bearing intergrowth microstructures in partially melted granulite-facies rocks. *Lithos* **56**, 97–110. doi: 10.1016/S0024-4937(00)00061-X

White RW and Powell R (2002) Melt loss and the preservation of granulite facies mineral assemblages. *Journal of Metamorphic Geology* **20**, 621–32. doi: 10.1046/j.1525-1314.2002.00206_20_7.x

White RW, Powell R, Holland TJB, Johnson TE and Green ECR (2014) New mineral activity–composition relations for thermodynamic calculations in metapelitic systems. *Journal of Metamorphic Geology* **32**, 261–86. doi: 10.1111/jmg.12071

Whitney DL and Evans BW (2010) Abbreviation for names of rock-forming minerals. *American Mineralogist* **95**, 185–7. doi: 10.2138/am.2010.3371

Williams MA, Kelsey DE and Rubatto D (2022) Thorium zoning in monazite: A case study from theIvrea–Verbano zone, NW Italy. *Journal of Metamorphic Geology* **40**, 1015–42. doi: 10.1111/jmg.12656

Wyllie PJ and Wolf MB (1993) Amphibolite dehydration-melting: sorting out the solidus. *Geological Society, London, Special Publications* **76**, 405–16. doi: 10.1144/GSL.SP.1993.076.01.20

Yakymchuk C (2020) Migmatites. In: Alderton D., Elias S.A. (Eds), *Enciclopedia of Geology* (2nd ed.), Academic press, 492–501. doi: 10.1016/B978-0-08-102908-4.00021-7

Zanoni D, Rebay G and Spalla MI (2016) Ocean floor and subduction record in the Zermatt-Saas rodingites, Valtournanche, Western Alps. *Journal of Metamorphic Geology* **34**(9), 941–61. doi: 10.1111/jmg.12215

Zucali M (2023) pyMinColab. https://github.com/mzucali/pyMinColab/ (accessed 14 July 2023).

Zucali M, Manzotti P, Diella V, Pesenti C, Risplendente A, Darling J and Engi M (2011) Permian tectonometamorphic evolution of the Dent-Blanche Unit (Austroalpine domain, Western Italian Alps). *Rendiconti online Società Geologica Italiana* **15**, 133–6.

https://doi.org/10.1017/S0016756824000037 Published online by Cambridge University Press